

Christoph Alexander Dösinger, BSc

Simulation of Angle-Resolved Photoemission Intensity Maps for Two-Dimensional Materials

MASTER'S THESIS

to achieve the university degree of
Diplom-Ingenieur
Master's degree programme: Technical Physics

submitted to

Graz University of Technology

Supervisor

Peter Puschnig, Assoc.-Prof. Dr.
Institute of Physics
University of Graz

Graz, March 2021

AFFIDAVIT

I declare that I have authored this thesis independently, that I have not used other than the declared sources/resources, and that I have explicitly indicated all material which has been quoted either literally or by content from the sources used. The text document uploaded to TUGRAZonline is identical to the present master's thesis.

Date, Signature

Abstract

Angle-resolved photoemission spectroscopy (ARPES) is the most direct experimental technique to investigate the electronic band structure of surfaces and layered materials. ARPES maps are routinely compared to results from ab-initio band structure calculations. However, simulations of photoemission cross-sections including transition matrix element effects which provide additional insights are rare, especially simulations that include spin-orbit coupling in the band structure calculation.

In this thesis, the electronic ground state is calculated using density functional theory (DFT). Based on the ground state wave function, angle-resolved photoemission intensity maps are simulated within the one-step model of photoemission, by modelling the final state of the photoelectron as a plane wave. This plane wave final state (PWFS) approach has proven to work surprisingly well for monolayers of organic molecules on metal surfaces. For this work, the approach is extended to include spin-orbit coupling (SOC). The results of the simulations are compared to experiments and calculations using a tight binding approach.

The method is applied to three classes of materials. First, the transition metal dichalcogenides (TMD) tungsten disulphide (WS_2) and tungsten diselenide (WSe_2), second, a monolayer of silver-tellurium on a silver-(111) surface ($\text{AgTe}/\text{Ag}(111)$), and, third, mono-layer and bilayer graphene. The simulations for the TMDs are able to correctly describe the ARPES intensities and the spin-splitting of the bands. However, results for $\text{AgTe}/\text{Ag}(111)$ show discrepancies to the experiments. It is shown that it is possible to include SOC in the PWFS approach, which can yield reliable results. However, further tests are needed.

Kurzzusammenfassung

Winkelaufgelöste Photoemissionsspektroskopie (ARPES) ist die direkteste experimentelle Methode um die elektronische Bandstruktur von Oberflächen und geschichteten Materialien zu untersuchen. Solche ARPES Experimente werden häufig mit ab-initio Bandstrukturrechnungen verglichen. Es gibt jedoch wenige Simulationen, bei denen auch Matrixelement-Effekte zur Berechnung der Photoemission berücksichtigt werden. Seltener noch sind Simulationen, welche auch Spin-Bahn Wechselwirkungen (SOC) in Betracht ziehen.

In dieser Abschlussarbeit wird zunächst der elektronische Grundzustand mit der Dichtefunktionaltheorie (DFT) berechnet. Basierend auf der Grundzustandswellenfunktion werden ARPES -Intensitäten mit dem sogenannten one-step Modell der Photoemission simuliert, wobei der Endzustand des Photoelektrons mit einer ebenen Welle genähert wird. In dieser Arbeit wird diese Methode so erweitert, um damit auch SOC zu berücksichtigen. Die Ergebnisse der Simulationen werden mit experimentellen Daten und einem tight-binding Modell verglichen.

Angewendet wird das Verfahren auf drei Klassen von Materialien: Erstens, die sogenannten transition metal dichalcogenides (TMD) Wolfram Disulfid (WS_2) und Wolfram Diselenid (WSe_2), zweitens, einer Monolage Silber Tellur auf einer Silber (111) Oberfläche ($AgTe/Ag(111)$), und drittens, ein- und doppelagigem Graphen. Die Simulationen für die TMDs sind in Übereinstimmung mit experimentellen Daten und geben auch die Aufspaltung der Bänder aufgrund der SOC korrekt wieder. Die Ergebnisse für $AgTe/Ag(111)$ zeigen jedoch Unterschiede zu den Experimenten. Es wird gezeigt, dass es möglich ist, SOC bei ARPES Simulationen zu berücksichtigen, und dass die Methode gute Ergebnisse liefern kann. Es sind jedoch weitere Tests notwendig.

Contents

1	Introduction	1
2	Theory	3
2.1	Introduction to Density Functional Theory	3
2.1.1	Theorem of Hohenberg and Kohn	4
2.1.2	Kohn-Sham Equations	5
2.1.3	Plane Wave Basis Set	7
2.2	Spin-orbit Coupling	9
2.3	Tight Binding - Method	11
2.4	Simulation of Angle-Resolved Photoemission Spectroscopy	12
2.4.1	Plane-Wave Final State Approach	13
2.4.2	Plane-Wave Final State Approach for SOC	14
2.4.3	ARPES Simulations within the TB Method	14
3	Results	16
3.1	Transition Metal Dichalcogenides: WS ₂ , WSe ₂	16
3.1.1	Structure of WS ₂ and WSe ₂	16
3.1.2	Electronic Structure	17
3.1.3	ARPES - Simulations	20
3.2	Monolayer of AgTe on Ag(111) Surface	26
3.2.1	Structure of AgTe/Ag(111)	27
3.2.2	Electronic Structure	28
3.2.3	ARPES - Simulations	28
3.3	Tight Binding Simulation for Graphene	33
3.3.1	Single Layer Graphene (SLG)	34
3.3.2	Bilayer Graphene in AA Stacking Order (BLG-AA)	38
3.3.3	Bilayer Graphene in AB Stacking Order (BLG-AB)	42
3.3.4	TB Models for BLG-AA and BLG-AB	46
4	Summary and Conclusion	48
	Appendix: Usage of chinook	50
	Bibliography	54

1 Introduction

Single layers of two-dimensional (2D) materials are a relatively new class of materials. Graphene, as the first of these materials has sparked interest due to its exceptional properties. One of which is the linear dispersion of the electronic band structure at the K -point near the Fermi-level. There the electrons can be described in terms of massless Dirac-fermions [1, 2].

Although graphene shows these interesting properties, it is not well suited for applications in electronic devices because it lacks a band gap. However, in recent years a number of other 2D materials have been investigated. One example are transition metal dichalcogenides (TMD), which form layered materials. Similar to graphite, many of these TMDs can also be synthesized in single layers [3–5]. By varying the transition metal atom or changing the dichalcogenide group, a whole range of properties are possible, where some of them show a sizeable band gap. Several of the TMDs, especially those containing tungsten or molybdenum also exhibit a large spin-orbit coupling (SOC) which offers novel applications in electronic devices [6–8]. However, to use such materials in electronic devices, it is essential to have a good understanding of their electronic properties. One of the best methods to experimentally determine the electronic band structure of a material is angular-resolved photoemission spectroscopy (ARPES). To interpret the experimental findings, it is important to be able to simulate ARPES experiments.

In this work two methods are used to simulate ARPES experiments. First, the plane-wave final state (PWFS) approach, which is already routinely done for organic thin films [9–11]. There the final state of the photoemitted electron is approximated by a free particle, that is, a plane wave. The initial states are Kohn-Sham orbitals obtained from a density functional theory (DFT) calculation. Second, a method based on a tight binding (TB) model is used as implemented in the python-package *chinook* [12].

The PWFS approach yields good results for simulating ARPES for organic thin films [13–15]. In this work, the approach is extended to materials showing strong SOC, where both the initial and final states, are described by spinors. A drawback of this method is, that it relies on an expensive DFT calculation where the computational costs only increase when taking SOC into account. One aim of this thesis is, to test whether the PWFS approach gives reliable results for materials showing strong SOC.

In contrast to the DFT-treatment, the TB-based method is a cost efficient and fast method to simulate an ARPES experiment. The method also can be easily extended to larger systems. But it must be kept in mind that its application depends on the availability of an accurate TB model. For small systems this method will be compared to the PWFS approach.

For this thesis, ARPES experiments will be simulated using the PWFS approach for the TMDs WS_2 and WSe_2 . Additionally simulations will be done for $AgTe/Ag(111)$. Here the simulations will be done twice, first, without SOC and, second, with SOC taken into account. Then the results will be compared to experimental data from literature. The aim is to asses, whether the PWFS approach yields reasonably results for these materials, that show strong SOC.

Alternatively, simulations will be done using *chinook*. The results of these simulations will be compared with the PWFS approach. The materials used in the simulations are single layer graphene and bilayer graphene in AA and AB stacking order. Aim of this part is, to asses the results yielded by *chinook*.

The thesis is organized as follows. Section 2 contains a short overview of the theories and methods used throughout this work. Following this, in Section 3, is a presentation of the results of the simulations together with short discussions. The last section contains a short summary of the main results of the simulations.

2 Theory

This section is dedicated to introducing the theories and models in this work. Density functional theory (DFT) and the tight binding (TB) method are used to calculate the electronic ground-states of two-dimensional (2D) systems. The resulting ground-state wave-functions are then used to simulate angle-resolved photoemission spectroscopy (ARPES) experiments. To this end, there will be a short introduction to DFT and the TB method. In addition to standard DFT there will be a short explanation of the theory of spin-orbit coupling and how it is treated in DFT. Finally, this section reviews the methods for simulating ARPES experiments based on both calculation methods (DFT, TB), employing the one step model of photoemission.

In this work, two different programs are used for the numerical calculations. For the DFT calculations the *Vienna ab-initio simulation package* (VASP) [16,17] is used. The TB calculations are done using the program *chinook* [12].

If not specified otherwise, atomic units are used:

$$\frac{e^2}{4\pi\epsilon_0} = m_e = \hbar = 1$$
$$c = \frac{1}{\alpha}, \quad \alpha = \frac{1}{137}$$

(m_e : electron mass, e : elementary charge, \hbar : Plank's constant, c : speed of light, α : fine-structure constant, ϵ_0 : vacuum permittivity).

2.1 Introduction to Density Functional Theory

DFT provides a way to calculate the ground-state of many-body systems such as condensed matter systems, which are comprised of the atomic nuclei and the electrons of a material. For such systems, the atomic nuclei are assumed as slowly moving compared to the electrons which is known as the Born-Oppenheimer Approximation [18]. Hence, it is possible to calculate the electronic ground-state for a fixed arrangement of the nuclei. The electronic ground-state then depends on the nuclear positions as parameters.

DFT is based the theorem of Hohenberg and Kohn [19] to reduce the many-body problem to calculating only the electron density of the ground-state. The ground-state density is then calculated self-consistently using the Kohn-Sham equations [20]. The following subsections will contain an explanation of these main points of DFT. The presentation will follow closely the lecture notes by Peter Puschnig [21].

2.1.1 Theorem of Hohenberg and Kohn

After applying the Born-Oppenheimer approximation, the Hamiltonian operator of an N - electron system consists of three parts [18]. The kinetic energy operator for the electrons \hat{T} , the energy \hat{V} of the electrons in the electrostatic potential $v(\vec{r})$ of the positively charged nuclei and the interaction between the electrons \hat{U} :

$$\hat{H} = -\frac{1}{2} \sum_{i=1}^N \Delta_i + \sum_{i=1}^N v(\vec{r}_i) + \frac{1}{2} \sum_{i,j \neq i}^N \frac{1}{|\vec{r}_i - \vec{r}_j|} = \hat{T} + \hat{V} + \hat{U} \quad (2.1)$$

where the \vec{r}_i and \vec{r}_j are the positions operators for the electrons i and j . The electrostatic potential of the nuclei $v(\vec{r})$ is often called the external potential. In Equation 2.1 only the electron-electron interaction is a two particle term that acts on two different electrons. The solution for the electronic problem and the corresponding stationary electronic states can then be obtained from the time-independent Schrödinger equation:

$$\hat{H} |\Psi\rangle = E |\Psi\rangle \quad (2.2)$$

Here $|\Psi\rangle$ stands for eigenstates of the Hamilton operator (Equation 2.1) with the corresponding eigenvalues E . In the following it is assumed that the ground-state $|\Psi_0\rangle$ to the lowest eigenvalue E_0 is non-degenerate:

$$\hat{H} |\Psi_0\rangle = E_0 |\Psi_0\rangle \quad (2.3)$$

Corresponding to the ground-state, the ground-state density can be defined:

$$n_0(\vec{r}) = N \cdot \int d^3r_2 \cdots \int d^3r_N |\Psi_0(\vec{r}, \vec{r}_2, \cdots \vec{r}_N)|^2 \quad (2.4)$$

The lemma of Hohenberg and Kohn states, that the external potential $v(\vec{r})$ caused by the Coulomb potential of the nuclei is uniquely defined by the ground-state density $n(\vec{r})$. This lemma can easily be shown by assuming that two different potentials v_1 and v_2 exist that give the same ground-state density. The assumption quickly leads to a contradiction, which proves the lemma to be true [19].

Another approach to obtain the ground-state energy E_0 is provided by the Rayleigh-Ritz variational principle. There the calculation is done by searching for the minimum of the expectation value of the total energy:

$$E_0 = \min_{|\Psi\rangle} \langle \Psi | \hat{H} | \Psi \rangle \quad (2.5)$$

Following the lemma of Hohenberg and Kohn, the minimization can be split into two parts. First minimizing the energy for a fixed electron density, which gives a functional for the energy $E[n(\vec{r})]$ depending on the density. Then this functional is minimized with respect to the electron density resulting in the ground-state energy E_0 :

$$E[n(\vec{r})] = \min_{|\Psi\rangle \rightarrow n(\vec{r})} \langle \Psi | \hat{H} | \Psi \rangle = F[n(\vec{r})] + \int d^3r v(\vec{r})n(\vec{r}) \quad (2.6)$$

$$E_0 = \min_{n(\vec{r})} E[n(\vec{r})] = \min_{n(\vec{r})} \left(F[n(\vec{r})] + \int d^3r v(\vec{r})n(\vec{r}) \right) \quad (2.7)$$

$$F[n(\vec{r})] = \min_{|\Psi\rangle \rightarrow n(\vec{r})} \langle \Psi | \hat{T} + \hat{U} | \Psi \rangle \quad (2.8)$$

Here, $F[n(\vec{r})]$ is the so-called universal functional and the integral $\int d^3r v(\vec{r})n(\vec{r})$ is the Coulomb energy of the electron density in the potential $v(\vec{r})$.

Finding the ground-state energy E_0 as the minimum of $E[n(\vec{r})]$ can be done by a variation of the density $n(\vec{r})$. This variation has to be done under the constraint that the number of electrons $N = \int d^3r n(\vec{r})$ remains constant, which is achieved by introducing the Lagrange-multiplier μ :

$$\begin{aligned} \frac{\delta}{\delta n(\vec{r})} \left\{ F[n(\vec{r})] + \int d^3r v(\vec{r})n(\vec{r}) - \mu \left(\int d^3r n(\vec{r}) - N \right) \right\} &= 0 \\ \Rightarrow \frac{\delta F[n(\vec{r})]}{\delta n(\vec{r})} + v(\vec{r}) &= \mu \end{aligned} \quad (2.9)$$

By using the density as main variable, Equations 2.6 and 2.7 reduce the ground-state problem from $3N$ degrees of freedom (Equation 2.2) to only 3 degrees of freedom. This reduces the computational effort dramatically, which makes ground-state calculations for larger systems possible. The drawback is, that the universal functional $F[n(\vec{r})]$, in general, is not known.

2.1.2 Kohn-Sham Equations

Although Equations 2.6 and 2.7 describing the theorem of Hohenberg and Kohn simplify the treatment of the electronic ground-state, solving the problem requires the knowledge of the yet unknown dependence of the the universal functional on the electron density. To overcome this problem Kohn and Sham introduced an auxiliary system of N non-interacting electrons. The external potential $v_a(\vec{r})$ of the auxiliary system is changed in such a way, that the resulting electron density $n_a(r)$ is equal to the electron density of the interacting system $n(\vec{r})$ [20]. The external potential of the interacting system is the bare Coulomb potential of the nuclei.

For the auxiliary non-interacting system, the electron-electron interaction \hat{U}_a vanishes. This way the Hamiltonian operator in Equation 2.1 reduces to a sum of one-particles operators:

$$\hat{H}_a = \hat{T} + \hat{V}_a = -\frac{1}{2} \sum_{i=1}^N \Delta_i + \sum_{i=1}^N v_a(\vec{r}_i) = \sum_{i=1}^N \hat{h}_a(\vec{r}_i) \quad (2.10)$$

The N -electron system can then be solved by simply calculating the single particle-states $\phi_i(r)$ from Equation 2.10. These states are then the Kohn-Sham orbitals and the single-particle equations are known as the Kohn-Sham equations [20]:

$$\left(-\frac{1}{2} \Delta_i + v_a(\vec{r}) \right) \cdot \phi_i(\vec{r}) = \epsilon_i \cdot \phi_i(\vec{r}) \quad (2.11)$$

From the single particle states one obtains the electron density by summing the contribution from the occupied states. The resulting density, is by construction, equal to the electron density of the interacting system:

$$n_a(\vec{r}) = n(\vec{r}) = \sum_{i=1}^N |\phi_i(\vec{r})|^2 \quad (2.12)$$

To be able to solve the Equations 2.11, the external potential of the auxiliary systems needs to be calculated. To this end, one again defines an energy functional $E_a[n_a(r)]$ in analogy to Equation 2.6

$$E[n_a(\vec{r})] = \min_{|\Phi\rangle \rightarrow n_a(\vec{r})} \langle \Phi | \hat{H}_a | \Phi \rangle = T_a[n_a(\vec{r})] + \int d^3r v_a(\vec{r}) n_a(\vec{r}), \quad (2.13)$$

where $|\Phi\rangle$ denotes the wave-function of the non-interacting system built from the Kohn-Sham orbitals ϕ_i . $T_a[n_a(\vec{r})]$ is the expectation value of the kinetic energy operator \hat{T} in the auxiliary system. Through minimizing the functional in Equation 2.13 one arrives at a similar form to Equation 2.9 with a different Lagrangian multiplier μ' :

$$\frac{\delta T_a[n_a(\vec{r})]}{\delta n_a(\vec{r})} + v_a(\vec{r}) = \mu' \quad (2.14)$$

Since the Lagrangian multipliers μ and μ' in Equations 2.9 and 2.14 can only differ by a constant that can be absorbed in the (auxiliary) potential $v_{(a)}(\vec{r})$, one can set these equations equal:

$$\frac{\delta F[n(\vec{r})]}{\delta n(\vec{r})} + v(\vec{r}) = \frac{\delta T_a[n(\vec{r})]}{\delta n(\vec{r})} + v_a(\vec{r}) \quad (2.15)$$

To continue from Equation 2.15, Kohn and Sham proposed a form for the universal functional [20]. The functional is split into three parts: the kinetic energy of the auxiliary system $T_a[n(\vec{r})]$, the classical electron-electron interaction as the Hartree energy $U_H[n(\vec{r})]$ and an unknown term, the exchange-correlation energy $E_{xc}[n(\vec{r})]$:

$$F[n(\vec{r})] = T_a[n(\vec{r})] + U_H[n(\vec{r})] + E_{xc}[n(\vec{r})] \quad (2.16)$$

Here, the Hartree energy functional is equal to the Coulomb repulsion of the electrons:

$$U_H[n(\vec{r})] = \int d^3r \int d^3r' \frac{n(\vec{r})n(\vec{r}')}{|\vec{r} - \vec{r}'|} \quad (2.17)$$

The Hartree energy represents the Coulomb interaction of a charge density purely based on classical interactions without quantum-mechanical effects.

Inserting Equation 2.16 for $F[n(\vec{r})]$ into Equation 2.15 one obtains an equation for the external potential $v_a(\vec{r})$ of the non-interacting auxiliary system by varying the electron density $n(\vec{r})$. The variation of the kinetic energy gets eliminated from the equation, the potential $v(\vec{r})$ is still the Coulomb potential of the nuclei:

$$v_a(\vec{r}) = v(\vec{r}) + \frac{\delta U_H[n(\vec{r})]}{\delta n(\vec{r})} + \frac{\delta E_{xc}[n(\vec{r})]}{\delta n(\vec{r})} = v(\vec{r}) + v_H(\vec{r}) + v_{xc}(\vec{r}) \quad (2.18)$$

Here, the variation of the exchange-correlation energy E_{xc} defines the exchange-correlation potential $v_{xc}(\vec{r})$. The variation of the Hartree energy U_H yields the Hartree potential $v_H(\vec{r})$:

$$v_H(\vec{r}) = \int d^3r' \frac{n(\vec{r}')}{|\vec{r} - \vec{r}'|} \quad (2.19)$$

By inserting Equation 2.18 into the Kohn-Sham Equations 2.11, one can solve for the single particle states. Since the Hartree energy and the exchange correlation energy themselves depend the electron density, the Kohn-Sham equations need to be solved iteratively. To solve the problem, the Equations 2.11, 2.12 and 2.18 are solved in a self-consistent manner using the following scheme:

0. Begin with an initial guess of N orbitals $\phi_i^{n=0}$ and calculate the initial electron density $n^{n=0}$ using Equation 2.12
1. calculate the external potential v_a^n from the density n^n (Equation 2.18)
2. solve the Kohn-Sham Equations 2.11, which results in new single particle states ϕ_i^{n+1}
3. construct the new density n^{n+1} from the state ϕ_i^{n+1}
4. repeat 1. through 4. until the density has converged (change of n^n , n^{n+1} smaller than a given threshold)

Up to this point DFT is still exact and provides a way to calculate the ground-state of an interacting N -electron system. But to be able to us the iterative scheme outlined above one has still to know the exchange-correlation functional $E_{xc}[n(\vec{r})]$. This functional, in practice, is unknown. To proceed, approximations to this unknown functional are made. In this work, the generalized gradient approximation (GGA) of Perdew, Burke and Ernzerhof is used (PBE-GGA) [22].

2.1.3 Plane Wave Basis Set

To do an actual calculation using DFT with the scheme outlined in the previous sections, one has to choose a basis set for the single-particle functions ϕ_i . For periodic systems, where the solutions must be Bloch waves [23], a natural choice for the basis are plane waves. To be able to treat three dimensional (3D) and two dimensional (2D) periodic systems simultaneously using the same approach, the 2D system is approximated in the repeated slab approach. There the 2D system is repeated in the third direction, however, with an added vacuum slab to separate the periodic replica of the 2D layer. This way the repeated slabs do not interact in this direction, but the system retains its periodicity in all three dimensions.

Following Bloch's theorem, Bloch waves $\chi_{\vec{k}}(\vec{r})$ corresponding to a specific wave-vector \vec{k} constitute of a plane wave $e^{i\vec{k}\vec{r}}$ modulated by a lattice-periodic function $u_{\vec{k}}(\vec{r})$ [23]:

$$\chi_{\vec{k}}(\vec{r}) = e^{i\vec{k}\vec{r}} \cdot u_{\vec{k}}(\vec{r}) \quad (2.20)$$

The lattice-periodic function $u_{\vec{k}}(\vec{r})$ has the same periodicity as the system. That means, it remains invariant under translation of one lattice vector \vec{R} of the system: $u_{\vec{k}}(\vec{r} + \vec{R}) = u_{\vec{k}}(\vec{r})$. Under the same transformation, the Bloch wave $\chi_{\vec{k}}(\vec{r})$ obtains a phase factor $e^{i\vec{k}\vec{R}}$. This allows one, to confine the wave-vectors \vec{k} to the first Brillouin zone (1.BZ) [24]. From the properties described above it follows, that the Bloch waves are eigenfunctions of the translational operator that causes translations in units of the lattice vectors. Since the translation operator commutes with the Hamiltonian operator of this system, Bloch waves are also eigenfunctions of the Hamiltonian operator. In general, they are not eigenfunctions of the momentum operator, which means that the wave-vector \vec{k} is not the true momentum of the electrons. \vec{k} represents the crystal momentum of the electrons in the periodic system [24].

The Kohn-Sham orbitals ϕ_i are then the plane waves as written in Equation 2.20. The index i of the orbitals refers to a compound index for the band-index n and the wave-vector \vec{k} :

$$\phi_i(\vec{r}) = \chi_{n,\vec{k}}(\vec{r}) = e^{i\vec{k}\vec{r}} \cdot u_{n,\vec{k}}(\vec{r}) \quad (2.21)$$

The vector \vec{k} runs through the whole 1.BZ, however, it is sufficient to sample the 1.BZ only at specific points. It is then necessary to test whether the resulting electron density and total energy are converged in respect of the chosen sampling of the 1.BZ.

A convenient choice for the lattice-periodic functions $u_{n,\vec{k}}(\vec{r})$ is to use plane waves (this approach gives the name for the basis set):

$$u_{n,\vec{k}}(\vec{r}) = \sum_{\vec{G}} c_{n,\vec{G}}(\vec{k}) e^{i\vec{G}\vec{r}} \quad (2.22)$$

The $c_{n,\vec{G}}(\vec{k})$ here are the plane wave coefficients. Since $u_{n,\vec{k}}(\vec{r})$ has to have the same periodicity as the system, the vectors \vec{G} need to be reciprocal lattice-vectors. In theory, the sum runs over all reciprocal space vectors, but for practical calculations the sum is restricted by the plane-wave cut-off to $|\vec{G}| \leq |\vec{G}_{cut}|$. This restricts then the number of plane wave coefficients, which directly determines the size of the matrices in the matrix eigenvalue problem, used to calculate the coefficients.

In a DFT calculation using a plane wave basis set the plane wave coefficients $c_{n,\vec{G}}(\vec{k})$ are determined. To be able to obtain reasonable results from such calculations, the plane-wave cut-off $|\vec{G}_{cut}|$ would have to be sufficiently large to correctly describe also the core-level electrons located near the nuclei. This makes calculations based on the plane-wave method difficult, since the number of plane-wave coefficients increases as $\mathcal{O}(|\vec{G}_{cut}|^3)$ and therefore the computational cost increases as $\mathcal{O}(|\vec{G}_{cut}|^9)$. To reduce computational costs various schemes have been implemented. This work uses to implementation of DFT used in the *Vienna ab-initio simulation package* (VASP) [16, 17]. VASP uses the projector augmented plane wave (PAW) method as described by Blöchl [25]. There the core-level states are projected out and only the valence electrons are considered in the calculation.

2.2 Spin-orbit Coupling

The Hamiltonian operator in Equation 2.1 describes the quantum mechanics of the a condensed matter system in a purely non-relativistic way. This description of the system excludes all effects of spin interactions. For this reason, to correctly calculate the effect of spin-orbit coupling (SOC), one needs a description of the electronic system in terms of relativistic quantum mechanics. There the Dirac equation describes the evolution of a quantum mechanical state of an electron [26].

In time-independent form the Dirac equation can be expressed as a set of two spinor equations [27]:

$$V\phi + c\vec{\sigma} \cdot \vec{p}\chi = E\phi \quad , \quad c\vec{\sigma} \cdot \vec{p}\phi + (V - 2c^2)\chi = E\chi \quad (2.23)$$

Here V is the potential energy of the electron, \vec{p} the momentum operator and $\vec{\sigma}_i$ the vector of the Pauli-matrices σ_x , σ_y and σ_z [26]:

$$\sigma_x = \begin{pmatrix} 0 & 1 \\ 1 & 0 \end{pmatrix} \quad , \quad \sigma_y = \begin{pmatrix} 0 & -i \\ i & 0 \end{pmatrix} \quad , \quad \sigma_z = \begin{pmatrix} 1 & 0 \\ 0 & -1 \end{pmatrix} \quad (2.24)$$

The ϕ and χ in Equation 2.23 are two component spinors, they are known as the large and small component of the four component spinor, respectively, described by the Dirac equation:

$$\Psi = \begin{pmatrix} \phi \\ \chi \end{pmatrix} \quad (2.25)$$

Keeping the four components of spinor Equation 2.25 is computationally unfavourable, since every component needs to be described by its own basis set. This would increase the memory demand and computational costs by a factor of four. One can reduce the number of spinor components by writing an effective two-component Hamiltonian, either by the so-called elimination of the small component (ESC) or the Foldy-Wouthuysen (FW) transformation [26, 27].

By using either of these methods, one obtains a relativistic Hamiltonian by doing a relativistic expansion in $\frac{1}{2c^2 - V}$. This leads to a zeroth order Hamilton operator that acts on a two component spinor [27]:

$$H^0 = V + \vec{\sigma} \cdot \vec{p} \frac{c^2}{2c^2 - V} \vec{\sigma} \cdot \vec{p} \quad (2.26)$$

This equation can be brought into another form, where the contribution to the Hamilton operator can be better understood:

$$H^0 = V + \vec{p} \frac{c^2}{2c^2 - V} \vec{p} + \frac{c^2}{2c^2 - V} \vec{\sigma} \cdot (\nabla V \times \vec{p}) \quad (2.27)$$

For small potentials V the first two terms of Equation 2.27 reduce to the non-relativistic Hamilton operator $H = \frac{1}{2}p^2 + V$. The third term causes a correction to the non-relativistic Hamiltonian depending on the momentum. Additionally, it will cause an

interaction between the spin-components via the Pauli-matrices $\vec{\sigma}$.

In this work, VASP is used for the DFT calculation. For implementing SOC, VASP uses a formulation of DFT for non-collinear spins [28, 29]. For non-collinear spins, DFT is expressed in form of 2×2 density matrices $n^{\alpha\beta}(\vec{r})$ [30], which is calculated from a two-component spinor:

$$n^{\alpha\beta}(\vec{r}) = \sum_{i=1}^N \phi_{\alpha i}(\vec{r}) \phi_{\beta i}^*(\vec{r}) \quad \alpha, \beta = 1, 2 \quad (2.28)$$

Here α and β refer to the components of the spinor which represent the spin up and the spin down part of the state $\vec{\phi}_i$, respectively.

$$\vec{\phi}_i = \begin{pmatrix} \phi_i^\uparrow \\ \phi_i^\downarrow \end{pmatrix} \quad (2.29)$$

The electron density $n(\vec{r})$ is calculated as the trace of the matrix $n^{\alpha\beta}(\vec{r})$. Projecting the density matrix onto the Pauli matrices $\vec{\sigma}$ leads to the magnetization $\vec{m}(\vec{r})$.

$$n(\vec{r}) = Tr[n^{\alpha\beta}(\vec{r})] = \sum_{\alpha=1,2} n^{\alpha\alpha}(\vec{r}) \quad (2.30)$$

$$\vec{m}(\vec{r}) = \sum_{\alpha\beta} n^{\alpha\beta}(\vec{r}) \cdot \vec{\sigma}^{\alpha\beta} \quad (2.31)$$

In this framework the energy of a state represented by the $\phi_{\alpha i}(\vec{r})$ can be calculated in a similar way as described in Section 2.1 [29]:

$$E = \sum_{\alpha=1,2} \sum_{i=1}^N \left\langle \phi_{\alpha i} \left| -\frac{1}{2} \Delta \right| \phi_{\alpha i} \right\rangle + \int d^3r v(\vec{r}) n(\vec{r}) + E_H[n(\vec{r})] + E_{xc}[n^{\alpha\beta}(\vec{r})], \quad (2.32)$$

where again $v(\vec{r})$ is the Coulomb potential of the nuclei, E_H and E_{xc} are the Hartree energy respectively the exchange-correlation energy. In this equation, only E_{xc} depends on the full density matrix. Equation 2.32 does not yet contain the spin-orbit coupling term.

For the implementation of SOC in VASP, it is assumed that the relativistic correction only acts in the regions near the nuclei [28]. The correction to the Hamilton operator (third term in Equation 2.27) is then implemented in the following form [28]:

$$H_{SOC}^{\alpha\beta} = \frac{1}{c^2 r} \left(1 - \frac{V(r)}{2c^2} \right)^{-2} \frac{dV(r)}{dr} \vec{\sigma}^{\alpha\beta} \cdot (\vec{r} \times \vec{p}) \quad (2.33)$$

Since $H_{SOC}^{\alpha\beta}$ acts only near the nuclei, the distance r in Equation 2.33 is understood to be relative to the center of the nearest core. The vector-product arises from the angular momentum of a state with respect to the center of the nucleus.

The expectation value of $H_{SOC}^{\alpha\beta}$ is then added to the energy defined in Equation 2.32.

2.3 Tight Binding - Method

As an efficient alternative to DFT, the tight binding (TB) method can be applied to calculate the ground state of condensed matter systems. For this method it is assumed, that the electrons are tightly bound to the atoms. This causes the overlap of the orbitals on different atoms to be negligible. For this reason it is advantageous to place, for example, hydrogen wave-functions at the atomic sites and build the the electronic state as a linear-combination of these atomic wave-functions [24].

For a periodic system the wave-function needs to fulfill Bloch's theorem, which can also be written in the following form [24, 31]:

$$\Psi(\vec{r} + \vec{R}) = e^{i\vec{k}\vec{R}}\Psi(\vec{r}) \quad (2.34)$$

Here \vec{r} is the position in the periodic system, where \vec{R} is a direct lattice vector of the system, and \vec{k} denotes the wave-vector of a Bloch wave as described in Section 2.1.3. One way to write the wave-function Ψ is to use plane waves, which leads to the Equation 2.20. Alternatively, it is possible to use an atomic wave function ϕ_n as a basis function to write a Bloch wave Φ_n [31]:

$$\Phi_n(\vec{k}, \vec{r}) = \frac{1}{\sqrt{N}} \sum_{\vec{R}_n} e^{i\vec{k}\vec{R}_n} \phi_n(\vec{r} - \vec{R}_n) \quad (2.35)$$

or, in ket-notation:

$$|\Phi_n(\vec{k})\rangle = \frac{1}{\sqrt{N}} \sum_{\vec{R}_n} e^{i\vec{k}\vec{R}_n} |\phi_n\rangle \quad , \quad \langle \vec{r} | \phi_n \rangle = \phi_n(\vec{r} - \vec{R}_n) \quad (2.36)$$

In these equations, the subscript n is a composite index referring to an atom in the unit cell of the lattice and an orbital thereof. The \vec{R}_n refer the atomic positions of the orbital n repeated through the crystal where N is the number of unit cells in the crystal. Writing the Φ_n as in Equation 2.36 fulfills the Bloch theorem Equation 2.34 [31].

The eigenstates Ψ_n of the periodic system can then be written as a linear combination of the of the Φ_n :

$$\Psi_n(\vec{k}, \vec{r}) = \sum_{n'} c_{nn'}(\vec{k}) \Phi_{n'}(\vec{k}, \vec{r}) \quad (2.37)$$

or, in ket-notation:

$$|\Psi_n(\vec{k})\rangle = \sum_{n'} c_{nn'}(\vec{k}) |\Phi_{n'}(\vec{k})\rangle \quad (2.38)$$

Since the Ψ_n are eigenfunctions of the periodic system, they fulfill the Schrödinger equation to the energy eigenvalue $E_n(\vec{k})$:

$$\hat{H}|\Psi_n(\vec{k})\rangle = E_n(\vec{k})|\Psi_n(\vec{k})\rangle \quad (2.39)$$

Using Equations 2.36 and 2.38 one can rewrite the Schrödinger equation 2.39 in matrix form. This leads to a generalized eigenvalue equation. In the second form the multiplications are understood as matrix-vector multiplication with the \vec{c}_n as the columns of

$c_{n''n}$:

$$\begin{aligned} \sum_{n''} \tilde{H}_{n'n''}(\vec{k}) c_{n''n}(\vec{k}) &= \sum_{n''} E_n(\vec{k}) \tilde{S}(\vec{k})_{n'n''}(\vec{k}) c_{n''n}(\vec{k}) \\ \tilde{H}(\vec{k}) \vec{c}_n(\vec{k}) &= E_n(\vec{k}) \tilde{S}(\vec{k}) \vec{c}_n(\vec{k}) \end{aligned} \quad (2.40)$$

Here, $\tilde{H}(\vec{k})$ is the expectation value of the Hamilton operator in the Bloch waves Φ_n . $\tilde{S}(\vec{k})$ is the overlap matrix of the different Bloch waves Φ_n . Those two matrices can be expressed in terms of the atomic basis-functions ϕ_n :

$$\tilde{H}_{nn'}(\vec{k}) = \langle \Phi_{n'} | \hat{H} | \Phi_n \rangle = \frac{1}{N} \sum_{\vec{R}_n, \vec{R}_{n'}} e^{ik(\vec{R}_n - \vec{R}_{n'})} H_{nn'} \quad , \quad H_{nn'} = \langle \phi_{n'} | \hat{H} | \phi_n \rangle \quad (2.41)$$

$$\tilde{S}_{nn'}(\vec{k}) = \langle \Phi_{n'} | \Phi_n \rangle = \frac{1}{N} \sum_{\vec{R}_n, \vec{R}_{n'}} e^{ik(\vec{R}_n - \vec{R}_{n'})} S_{nn'} \quad , \quad S_{nn'} = \langle \phi_{n'} | \phi_n \rangle \quad (2.42)$$

The diagonal elements of $H_{nn'}$ are often referred to as on-site energies and the off-diagonal elements are the hopping integrals between the basis states ϕ_n .

Since the orbitals are decaying rapidly as a function of the distance from the center of the respective site, the overlap $S_{nn'}$ is close to unity. If $S_{nn'}$ is assumed to be equal to the unity, the generalized eigenvalue problem Equation 2.40 reduces to a standard eigenvalue problem: $(\tilde{H}(\vec{k}) - E_n(\vec{k})) \vec{c}_n(\vec{k}) = 0$ which can be easily solved. In this way, calculating the bandstructure is equal to calculating the eigenvalues of the hopping matrix at the different wave-vectors \vec{k} .

In practice, the basis states are restricted to orbitals on atomic sites in the chosen unit cell. Since hopping between orbitals predominantly takes place between nearest neighbours, the sum over \vec{R}_n in Equations 2.41 and 2.42 can be restricted to the neighbouring sites of the respective orbital n .

In this work, the hopping integrals are not calculated explicitly. The values for the hopping integrals are obtained by fitting the resulting $E_n(\vec{k})$ to results from a DFT calculation.

2.4 Simulation of Angle-Resolved Photoemission Spectroscopy

Angle resolved photoemission spectroscopy (ARPES) is one of the most direct experimental methods to probe for the electronic structure of a material or surface. In the experiments, photons of a specific energy ω and polarization $\vec{\epsilon}$ are used to excite electrons from a surface. These emitted electrons are then measured angle and energy resolved. Measuring these quantities simultaneously allows to reconstruct the band structure of the material from the measured photoelectron intensity maps.

In this work, ARPES is simulated within the one-step model of photoemission [32]. Following Fermi's golden rule the energy and angle dependent photoelectron intensity is

proportional to the matrix element of the initial state $|i\rangle$ and the final state $|f\rangle$ with interaction with the photon-field [33]:

$$I(\theta, \phi, E_{kin}; \omega) \propto \sum_i \left| \left\langle f | \vec{A} \cdot \vec{p} | i \right\rangle \right|^2 \delta(\omega - E_i - \Phi - E_{kin}) \quad (2.43)$$

Here the angles θ , ϕ and the kinetic energy E_{kin} characterize the direction and kinetic energy of the outgoing electron. Alternatively, the emitted electron can be described by momentum components parallel k_{\parallel} and perpendicular k_{\perp} to the surface, respectively. In minimal coupling and Coulomb gauge the interaction between the photon field and the electron is given by the product of the vector potential with the momentum operator $\vec{A} \cdot \vec{p}$. In the dipole-approximation, the vector potential of the incoming photons reduces to the polarization vector $\vec{A} = \vec{\epsilon}$. In Equation 2.43, E_{kin} refers to the kinetic energy of the photoelectron, E_i is the binding energy of the initial state $|i\rangle$ and Φ is the work-function. The Dirac-delta guarantees energy conservation in the photoemission process [34],

$$E_{kin} = \omega - E_i - \Phi. \quad (2.44)$$

In the following sections three approaches will be presented. They differ in the form of the initial states. Two methods are based on Kohn-Sham orbitals resulting from a DFT calculation. The third approach is based on a TB description of the initial states. All three methods approximate the final state as a plane wave.

2.4.1 Plane-Wave Final State Approach

The plane-wave final state (PWFS) approach uses a plane wave $e^{i\vec{k}\vec{r}}$ to approximate the final state of the photoelectron. As initial states, Kohn-Sham orbitals resulting from a DFT calculation are used. Here the Kohn-Sham orbitals are written in a plane-wave basis (Equations 2.21,2.22). Using these descriptions of the initial and final states, the photoelectron intensity in Equation 2.43 simplifies to the following form [33]:

$$I(\vec{k}, E_{kin}; \omega) \propto |\vec{A} \cdot \vec{k}| \sum_{i, \vec{q}} \left| \left\langle e^{i\vec{k}\vec{r}} | \chi_{i, \vec{q}}(\vec{r}) \right\rangle \right|^2 \delta(\omega - E_{i, \vec{q}} - \Phi - E_{kin}) \quad (2.45)$$

Thus, the photoelectron intensity splits into two parts, first the polarization factor $\vec{A} \cdot \vec{k}$ that modulates the matrix-elements $\left| \left\langle e^{i\vec{k}\vec{r}} | \chi_{i, \vec{q}}(\vec{r}) \right\rangle \right|$, and second, the contribution of the matrix-element between the initial states and the final states. The matrix-elements must be summed over the different Bloch-states for the momenta \vec{q} in the first Brillouin zone and the occupied bands i .

The choice of the k -mesh sampling the 1.BZ used to calculate the Kohn-Sham orbitals $|\chi_{i, \vec{q}}\rangle$ influences the resolution of the simulated photoemission intensity maps. The resolution can be calculated for each direction separately as: $\Delta k_i = \frac{2\pi}{a_i * n_i}$. Here a_i is the size of the unit cell in i direction and n_i is the number of sampling points in the same direction. Δk_i should than be smaller than the chosen resolution for all directions i . This restriction on the resolution also applies for PWFS approach for SOC described in the following section.

2.4.2 Plane-Wave Final State Approach for SOC

The PWFS approach for SOC builds on the PWFS approach described in the last section. Since the description of the photoemission process is in first order spin-independent [35], it is possible to directly use Equation 2.45 also for a spin-dependent description of ARPES.

To include spin-dependence of the initial $|i\rangle$ and final states $|f\rangle$, they are written in spinor form:

$$|i\rangle = \begin{pmatrix} |i^\uparrow\rangle \\ |i^\downarrow\rangle \end{pmatrix} = \begin{pmatrix} \chi_{i,\vec{q}}^\uparrow(\vec{r}) \\ \chi_{i,\vec{q}}^\downarrow(\vec{r}) \end{pmatrix} \quad (2.46)$$

$$|f\rangle = \begin{pmatrix} |f^\uparrow\rangle \\ |f^\downarrow\rangle \end{pmatrix} = \begin{pmatrix} e^{i\vec{k}\vec{r},\uparrow} \\ e^{i\vec{k}\vec{r},\downarrow} \end{pmatrix} \quad (2.47)$$

Inserting Equations 2.46 and 2.47 into Equation 2.45 then gives the total photoemission intensity as follows:

$$I(\vec{k}, E_{kin}; \omega) \propto |\vec{A} \cdot \vec{k}| \sum_{i,\vec{q}} \left| \left\langle e^{i\vec{k}\vec{r},\uparrow} | \chi_{i,\vec{q}}^\uparrow(\vec{r}) \right\rangle + \left\langle e^{i\vec{k}\vec{r},\downarrow} | \chi_{i,\vec{q}}^\downarrow(\vec{r}) \right\rangle \right|^2 \delta(\omega - E_{i,\vec{q}} - \Phi - E_{kin}) \quad (2.48)$$

Thus, the intensity can be viewed as a sum of the contributions from the spin-up and spin-down electrons. Since the spins give different contributions to the total intensity, the spin-polarization P can be defined as the difference of the signals from spin-up and spin-down:

$$P(\vec{k}, E_{kin}; \omega) \propto |\vec{A} \cdot \vec{k}| \sum_{i,\vec{q}} \left\{ \left| \left\langle e^{i\vec{k}\vec{r},\uparrow} | \chi_{i,\vec{q}}^\uparrow(\vec{r}) \right\rangle \right|^2 - \left| \left\langle e^{i\vec{k}\vec{r},\downarrow} | \chi_{i,\vec{q}}^\downarrow(\vec{r}) \right\rangle \right|^2 \right\} \delta(\omega - E_{i,\vec{q}} - \Phi - E_{kin}) \quad (2.49)$$

2.4.3 ARPES Simulations within the TB Method

The electronic states resulting from a TB calculation are given as a linear superposition of the states used to set up the tight binding model. Following Section 2.3, the initial state for the simulation of an ARPES experiment can be written in the following way [12]:

$$|i\rangle = |\Phi_n(k)\rangle = \sum_j b_j^n(k) |\phi_j\rangle \quad (2.50)$$

Here n is the band-index of the the initial state, b_j^n is a general coefficient of the linear superposition of the hydrogen wave-functions $|\phi_j\rangle$ used in the TB model. The sum j runs over all basis-states of the model.

In order to evaluate the matrix elements for initial states in an atom-centered basis, it is advantageous to convert the plane wave final state from Cartesian coordinates to

spherical coordinates. For this purpose, the plane waves are described in the Rayleigh expansion, where the plane waves are expanded in spherical harmonics [12, 36]

$$e^{i\vec{k}\vec{r}} = 4\pi \sum_{L=0}^{\infty} \sum_{M=-L}^L i^L j_L(k \cdot \vec{r}) Y_{L,M}(\hat{r}) Y_{L,M}^*(\hat{k}) \quad (2.51)$$

In this expansion $Y_{L,M}$ are the spherical harmonics for the unit vectors \vec{r} , respectively \vec{k} in spherical coordinates. The j_L are the spherical Bessel-functions.

Writing the final state as a Rayleigh expansion of a plane wave simplifies the calculation of the matrix-element to a product of Gaunt-coefficients with the integrals of the radial parts of the final and initial states [12]. The Gaunt-coefficients result from an integral over three spherical harmonics.

3 Results

3.1 Transition Metal Dichalcogenides: WS_2 , WSe_2

Transition metal dichalcogenides (TMD) are a class of materials, that similar to graphene form 2D-layered structures [4, 5]. Opposed to graphene, these single layer TMDs show a variety of different electronic properties allowing for novel applications in electronic devices [3]. Some materials of this class additionally exhibit strong spin-orbit coupling (SOC). The TMDs tungsten-disulphide (WS_2) and tungsten-diselenide (WSe_2) are two representatives of these materials, where the SOC causes a large spin-splitting of the top valence bands at the K -point at the edge of the first Brillouin zone.

Since WS_2 and WSe_2 are such materials, the implementation of SOC in the VASP is used. Therefore, program used to simulate ARPES experiments needs to be extended to spin-resolved ARPES-simulations. The plane wave final state approximation for simulating angular resolved photoemission spectroscopy (ARPES) experiments, as described in Section 2.4.1 has yielded satisfying results for organic molecules on metal surfaces [10, 11]. To test whether this simple theoretical approach is also applicable for materials containing heavier elements that show strong spin-orbit coupling, simulations are done and compared to experimental data from literature.

For the simulations, first a geometry relaxation of the structures of WS_2 and WSe_2 is done. Then the electronic band structure is calculated for both materials. Finally, in the last part of this section ARPES simulations are done, which are then compared to experiments.

3.1.1 Structure of WS_2 and WSe_2

Bulk transition metal dichalcogenides (TMD) are layered materials where the interlayer bonding arises primarily from van-der-Waals forces. Each layer is comprised of three sub-layers as shown in Figure 3.1. The middle sublayer consists of a transition metal such as tungsten (W) and the top and bottom sublayers are built up from of 6th group elements, for example sulphur (S) or selen (Se). Several types of such bulk-TMDs like WS_2 and WSe_2 can be exfoliated to or synthesized in single layers [3, 5]. The most stable phase of single layer WS_2 and single layer WSe_2 has the so-called 2H-structure shown in Figure 3.1 [3, 8]. As can be seen in Figure 3.1b, the atoms in the top and bottom sublayers are above each other, which is characteristic to the 2H-structure as opposed to other structures.

As a starting point for all subsequent calculations, a geometry relaxation is done, where the initial values of the structural parameters used for the relaxation are taken from

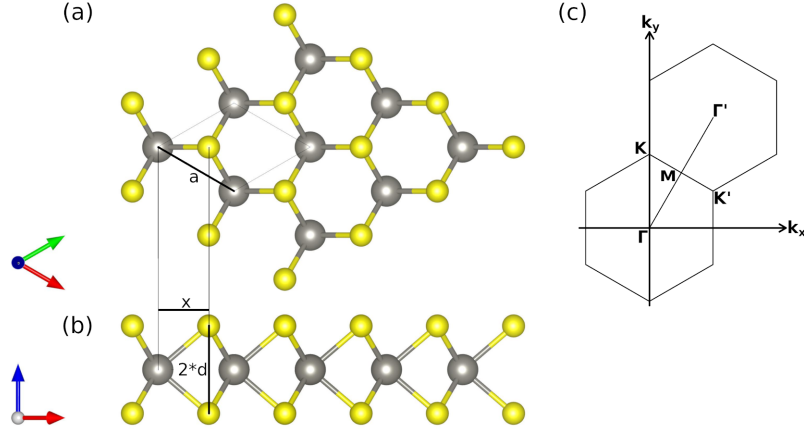


Figure 3.1: 2H-structure of transition metal dichalcogenides, yellow: dichalcogenide-atoms (S, Se); grey: transition metal-atoms (W). (a) Top view of the structure. (b) Side view, the atoms of the dichalcogenide atoms below and above the metal layer are directly above each other. The structural parameters are listed in Table 3.1. (c) Two dimensional Brillouin zone with high symmetry points.

Ref. [3]. The atomic position of WS_2 and WSe_2 are relaxed until forces are smaller than $0.01 \text{ eV}\text{\AA}^{-1}$. The PBE-GGA functional is used for the relaxation and all subsequent DFT calculations. Table 3.1 lists the relaxed structural parameters of WS_2 and WSe_2 , as marked in Figure 3.1. Additionally, Table 3.1 provides values for the structural parameters measured in experiments and results from other calculations from literature. The resulting lattice constants of 3.17 \AA for WS_2 and 3.31 \AA for WSe_2 are in good agreement with experimental results [4, 37, 38]. The result for the thickness of a single layer, which for both materials is similar to the lattice constant, also agrees with the measurements. For WSe_2 the experimental values for the structural parameters correspond to the bulk material.

3.1.2 Electronic Structure

The electronic band structures of WS_2 and WSe_2 are calculated for the respective relaxed structures. A k -mesh of $30 \times 30 \times 1$ points is used to sample the first Brillouin zone in the calculations. To be able to compare the band structure calculation with simulated and experimental ARPES-data, the calculations are done in two modes: without SOC and with SOC. This way, also the effects of SOC can easily be analysed. In Figures 3.2 and 3.3 (page 19) the solid lines give the band structure without SOC and the dashed lines show the band structure with SOC included. Tables 3.2 and 3.3 (page 20) summarise the most relevant properties of the electronic band structures of WS_2 and WSe_2

Table 3.1: Structural parameters a , d , x for WS_2 and WSe_2 as marked in Figure 3.1
 $(x = \frac{a}{\sqrt{3}})$

	present work		experiments		other calculations [3]	
	WS_2	WSe_2	WS_2	WSe_2 (bulk)	WS_2	WSe_2
$a / \text{\AA}$	3.17	3.31	3.2 [4]	3.28 [38]	3.13	3.25
$d / \text{\AA}$	1.57	1.68	1.6 ± 0.4 [37]	1.67 ± 0.005 [38]	1.56	1.67
$x / \text{\AA}$	1.83	1.91	–	–	1.84	1.88

calculated with and without including SOC. The tables also include results obtained in experiments, except for the bandgap of single layer WS_2 , where no experimental data was found in literature.

For both materials and both types of calculations the valence band maximum is positioned at the K -point. There is a second maximum at the Γ -point that is lower in energy. This energy difference between these two maxima is labeled as $\Delta_{K\Gamma}$ in Tables 3.2 and 3.3. $\Delta_{K\Gamma}$ is underestimated by the calculations if SOC is not considered. When including SOC, the calculated $\Delta_{K\Gamma}$ grows by about half the value of the spin-splitting at the K -point. The $\Delta_{K\Gamma}$ calculated for WSe_2 of 539 meV fits to the experimental value of 560 meV, whereas, for WS_2 the calculated value of 307 meV is around 100 meV larger than the value measured in experiment (Table 3.2).

We first focus on the effect of spin-polarization on the valence band structure. The most obvious difference is the splitting of the top-valence band at the K -point in reciprocal space, which is described as Δ_K in Tables 3.2 and 3.3. This spin-splitting was also measured in experiments using ARPES [7, 37, 39, 40] (e.g. Figure 3.7a page 24) and gives a measure for the strength of the SOC. Δ_K is calculated to a value of 403 meV for WS_2 and 436 meV for WSe_2 . The calculations somewhat underestimate the results of the experiments.

Next we concentrate on the influence of SOC on the bandgap. As expected, both materials show a sizeable bandgap [40, 41], where the size of the bandgap changes when including SOC (Tables 3.2, 3.3). For both materials the valence band maximum is around the K -point in reciprocal space (Figures 3.2, 3.3). The conduction band minimum lies at the K -point when not including SOC. If SOC is included in the calculations, there is a second minimum between the Γ - and K -point that has nearly the same energy as the minimum at the K -point. Thus, both materials are predicted to be direct bandgap semiconductors when not including SOC in the calculation. For WSe_2 the calculation including SOC underestimates the bandgap by around 0.6 eV compared to experimental values. The value for the bandgap of WSe_2 of 1.95 eV was measured using a STM [40].

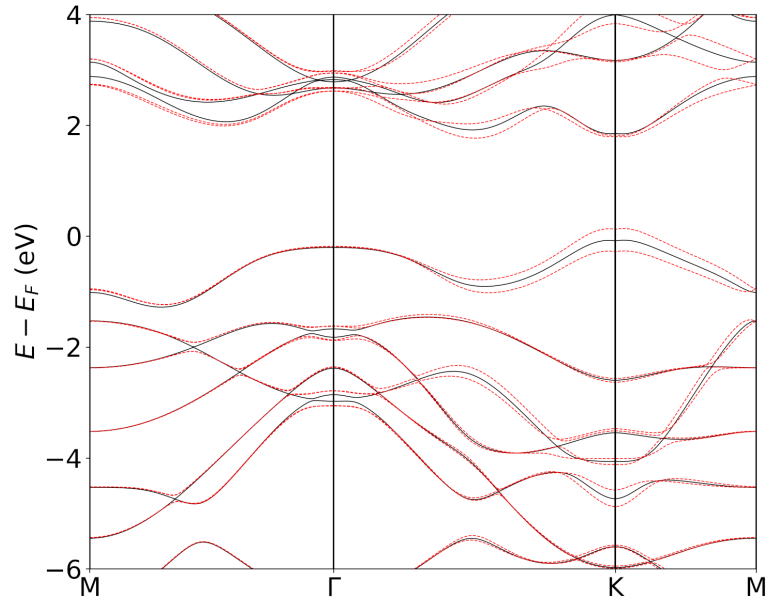


Figure 3.2: Band structure of WS_2 without SOC (full lines) and with SOC (dashed lines). The energies are aligned to the Fermi-level of the calculation without SOC.

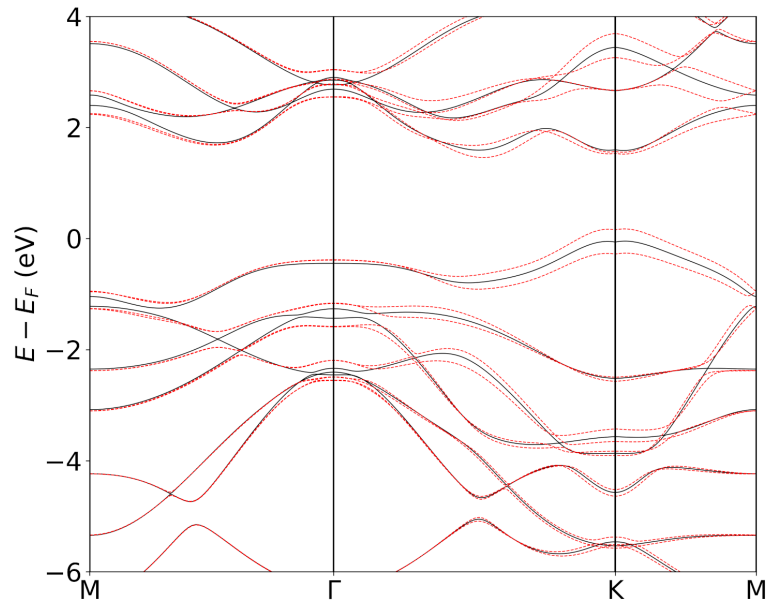


Figure 3.3: Band structure of WSe_2 without SOC (full lines) and with SOC (dashed lines). The energies are aligned to the Fermi-level of the calculation without SOC.

Table 3.2: characteristics of the electronic band structure of WS₂;

	no SOC	with SOC	experiment
fundamental gap / eV	1.9	1.6	–
$\Delta_{K\Gamma}$ / meV	117	307	200 [41]
Δ_K / meV	–	403	420 [37]

Table 3.3: characteristics of the electronic band structure of WSe₂;

	no spin-orbit coupling	with spin-orbit coupling	experiment [40]
fundamental gap / eV	1.6	1.3	1.95 ± 0.04
$\Delta_{K\Gamma}$ / meV	383	539	560
Δ_K / meV	–	436	475

3.1.3 ARPES - Simulations

In this section, simulated ARPES intensity maps are compared to experimental ARPES-data which have been taken from References [39,42,43]. The simulations for both TMDs are based on VASP - calculations for free-standing single layers of the respective material. The simulations are performed, first, without and, second, with SOC. A $45 \times 45 \times 7$ k -mesh for sampling the first Brillouin zone is used for the simulations, yielding a resolution of less than 0.05 \AA^{-1} of the simulated ARPES intensity maps. Finally, the details of the simulations, such as the photon-energy or the angle of incidence, are adjusted to the available information about the experimental setups.

ARPES WS₂. For this section band maps in k_x (Γ - M) and k_y (Γ - K) direction are simulated (Figure 3.4) as well as momentum maps for several binding energies (Figures 3.5 and 3.6). The simulated intensity maps are compared to experimental data from Ref. [42]. Since the simulations are done for a free-standing mono-layer of WS₂ and the experiment was done for a mono-layer on a TiO₂ surface the binding energies are shifted. This shift of the binding energies in the experiment is caused by a shift of the Fermi-level due to the influence of the substrate. The ARPES experiments of Ref. [42] were conducted for a mono-layer of WS₂ on TiO₂ (100) surface. For the experiments photon-energy of 90 eV was used with angle of incidence of 55°.

Figure 3.4 shows the simulated and measured band maps of WS₂. The left column shows the Γ - M direction, the right column the Γ - K direction. In the top row are experimental maps [42]. The middle row shows the simulations without SOC, while the bottom row contains the maps simulated with SOC. Note that these maps are calculated from the sum of both spin-channels (up, down). The lines inset in the the simulated maps mark the M -point, respectively the K -point in reciprocal space.

The simulated band maps are consistent with the calculated band structure of WS₂

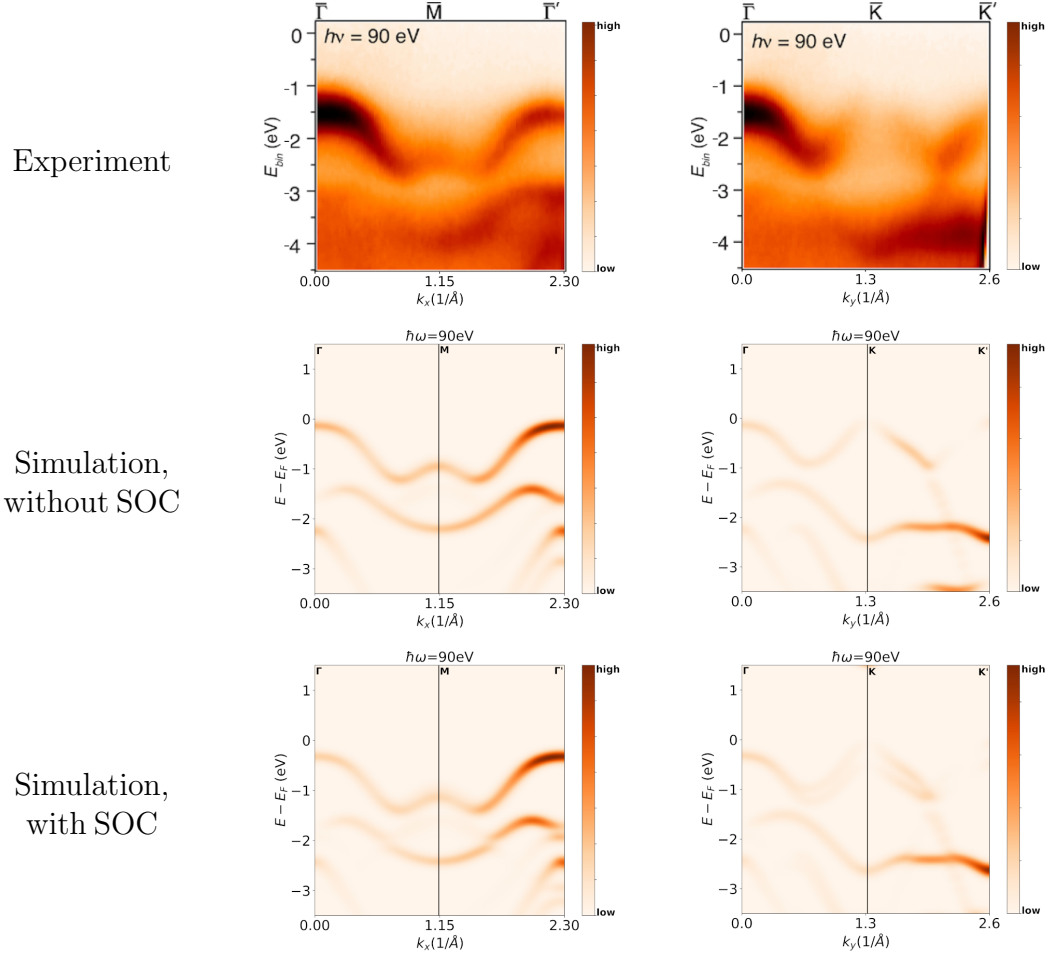


Figure 3.4: Band maps of WS_2 , photon-energy 90 eV; top row: experiment taken from Reference [42]; left column: Γ - M direction in momentum space; right column: Γ - K direction in momentum space; middle row: simulations without SOC, bottom row: simulations with SOC

shown in Figure 3.2. For both simulations the resulting intensity distribution is similar. The major difference between the simulated maps is the energy splitting of the top-valence band at the K -point due to spin-orbit interactions. The form of the simulated maps coincide with the measured maps, however, the photoemission intensity distributions do not agree entirely. In agreement with the experiment, the simulated maps show the same low photoemission intensity from the top valence band at the boundary of the first Brillouin zone at the K - and M -points. Due to the low intensity of the experimental maps it is not possible to distinguish the two spin-split bands at the K -point. However, the experimental map for the Γ - M show high intensity at the Γ -point and low intensity at the Γ' -point in the second Brillouin zone for the top valence band. Thus, the distribution of the photoemission intensity for the top valence band between the Γ

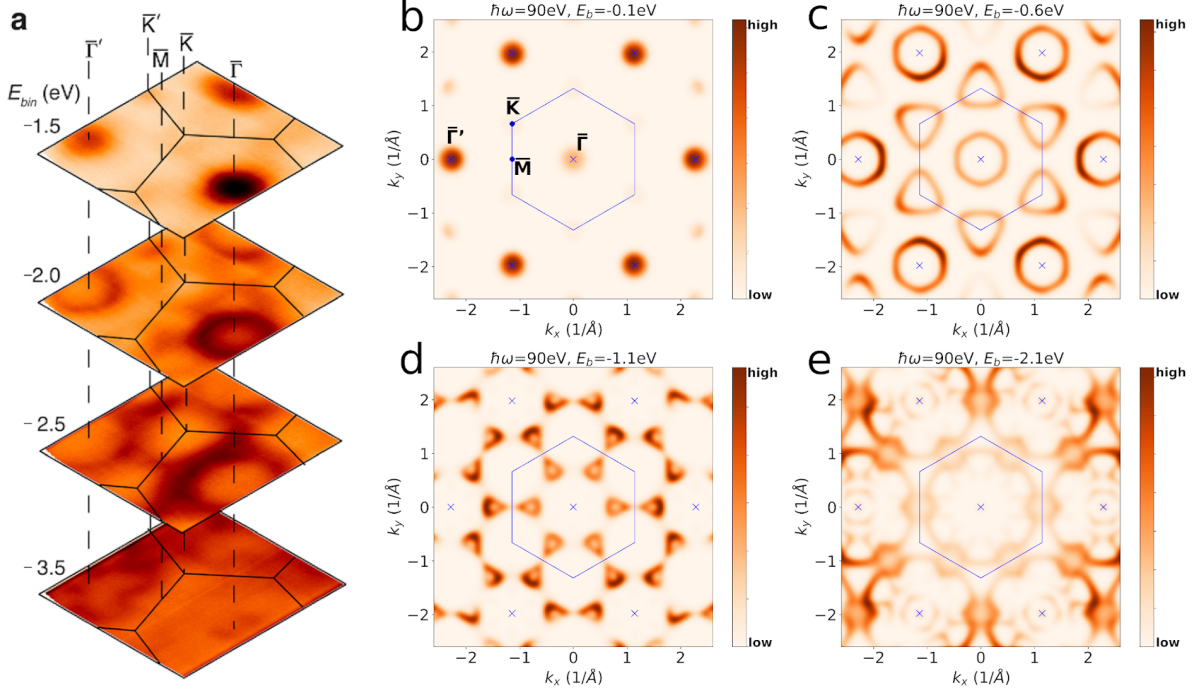


Figure 3.5: Momentum maps of WS_2 , photon-energy 90 eV; a: Experiment taken from Ref. [42], binding energies: 1.5 eV, 2.0 eV, 2.5 eV, 3.5 eV; b-e: simulated momentum maps as described in the text, spin-orbit coupling not included, binding energies: -0.1 eV, -0.6 eV, -1.1 eV, -2.1 eV, blue line: boundary of the first Brillouin zone, blue cross: Γ -point inside first Brillouin zone (center) and outside of first Brillouin zone

and Γ' point appears to be reversed for the simulated maps. On the other hand, for the second highest band the intensity distributions of the simulated and the experimental band maps agree for both directions (Γ - K , Γ - M).

In Figure 3.5, we now focus on the comparison of the momentum maps at selected binding energies. Panel a shows experimental results again taken from Reference [42], while panels b-e contain the corresponding simulated maps without SOC. In Figures 3.6a-d the momentum maps simulated with spin-orbit coupling are shown. These maps are calculated from the sum of the of the spin-channels (up + down). The measurements shown in Figure 3.5a are done at binding energies of -1.5 eV, -2.0 eV, -2.5 eV and -3.5 eV. The simulations of the momentum maps for -0.1 eV, -0.6 eV, -1.1 eV and -2.1 eV correspond best to the respective measured maps. This shift of the binding energy is due to the influence of the substrate as described before.

At the lowest binding energy of -1.5 eV of the experimental map there are contributions only from the K -point and the Γ -/ Γ' -points in-/outside the first Brillouin zone. These contributions form points that open up to circles around the high symmetry points for higher binding energies. In the experimental maps at a binding energy of -2.5 eV, this

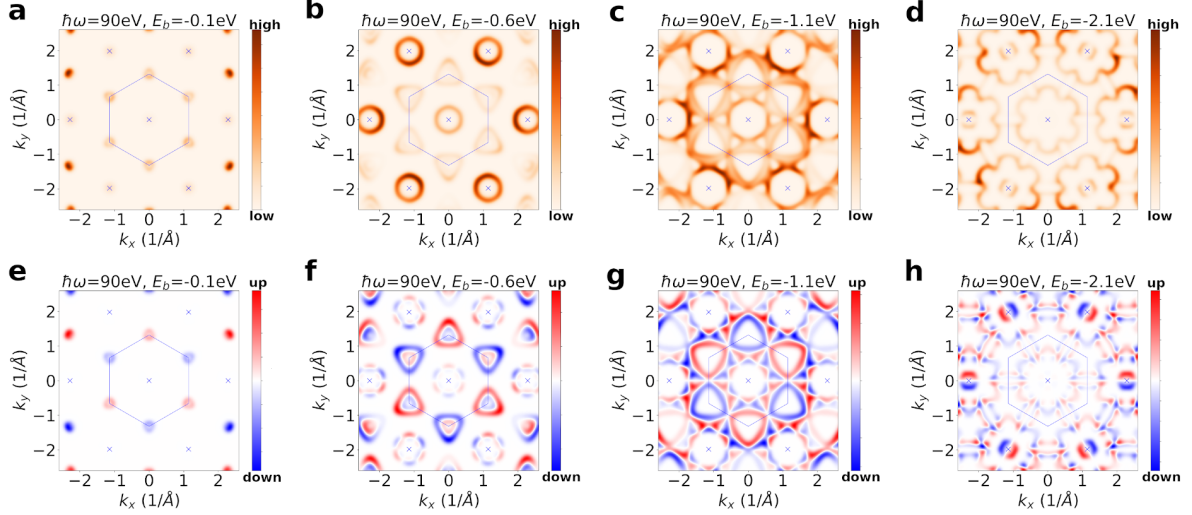


Figure 3.6: Momentum maps of WS_2 , photon-energy 90 eV; with SOC, the maps correspond to the ones in Figure 3.5; a-d: sum of the spin-channels; e-h: spin polarization of the simulated maps; blue line: boundary of the first Brillouin zone, blue cross: Γ -point inside first Brillouin zone (center) and outside of first Brillouin zone

ringlike structures start to touch. Similar to the experimental band maps, the momentum maps show higher photoemission intensity originating from inside the first Brillouin zone than from outside for low binding energies. For the highest binding energy of -3.5 eV this distribution is reversed.

When taking into account the rigid shift of binding energies discussed above, the simulated maps show similar structures as the experiments. Comparing the photoemission at the Γ respectively the Γ' point with the the experiments show that the ratio of the intensities are reversed for the lower binding energies. This is similar to the band maps discussed before. For the highest binding energy (experiment: -3.5 eV, simulation: -2.1 eV) the simulations are in good agreement with the experiment although the simulation shows far more details than the experimental map.

When comparing the two different simulations, with and without SOC, respectively, they show similar structures. At the binding energy of -0.6 eV the ringlike structures get the structure of a double ring when spin-orbit coupling is taken into account. The rings can be best distinguished in the maps for the polarization (Figure 3.6f). This double ring structure lowers the contributions of each single ring which might conform better with the experiment. For the higher binding energy of -1.1 eV the separate structures around the K -point (Figure 3.5d) change to closed forms (Figure 3.6c). These closed forms can also be seen in the experiment (Figure 3.5a, -2.5 eV).

Figures 3.6e-h show simulations for the spin-polarization of the ARPES-signal as defined in Section 2.4.2. These maps shown here correspond to the momentum maps in Figures 3.6a-d (directly above). The spin-polarization is equivalent to the difference of the signals from the two spin-channels (up $-$ down). The first three maps show that

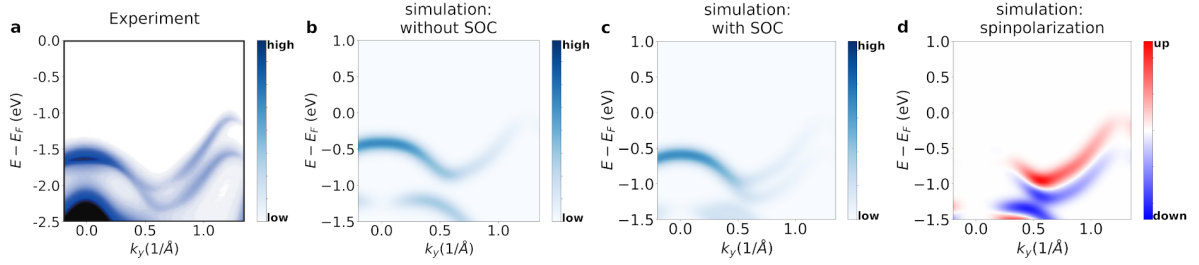


Figure 3.7: Band maps of WSe_2 in Γ - K direction, K -point at 1.26 \AA^{-1} , photon-energy 70 eV; a: Experiment taken from Ref. [39]; b-c: simulation done as described in the text, b: no spin-orbit interaction, c: with spin-orbit interaction, d: spin-polarization

the signal at the K -points is spin-polarized, and that the polarization of inequivalent K -points has different signs. At the binding energy of -0.6 eV , the ringlike structures around the K -points show areas of different polarization. This corresponds to the double rings already described above for the simulations of the total ARPES signal. It also corresponds to the spin-splitting visible in the band structure and ARPES band maps of WS_2 . At lower binding energies ($E_B = -2.1 \text{ eV}$, Figure 3.6h), the simulation shows a spin-polarized signal at the Γ -points outside the first Brillouin zone (crosses in figure 3.6). This polarization is suppressed inside the first Brillouin zone (Γ) but visible outside (Γ'). This polarization coincides with a partition of the signal around these points in reciprocal space into two parts that are also observed in the simulated momentum maps (Figures 3.6d, 3.4e).

ARPES WSe_2 In this paragraph simulations of ARPES band maps are calculated for a free-standing single layer of WSe_2 . These simulations are then compared to experimental data from Refs. [39, 43]. In both experiments a single layer WSe_2 has been used, albeit, on different substrates. Ref. [39] used a single layer of WSe_2 grown on bilayer graphene with a photon-energy of 70 eV, while Ref. [43] utilized a mono-layer of WSe_2 on a SiO_2 terminated silicon surface and a photon-energy of 74 eV at an angle of incidence of 45° .

In the simulations the parameters for the photon-energy and the polarization were adjusted to reflect the parameters used in both experiments.

Regarding the spin-splitting of the top-most valence band at the K -point both references agree on values of $(513 \pm 10) \text{ meV}$ [39] and $\sim 470 \text{ meV}$ [43], respectively. These values should be compared with the calculated value of 436 meV , which somewhat underestimates the measured values. The simulations in Γ - K direction (Figures 3.7a, 3.8 left column) and along the boundary of the first Brillouin zone in K - M - K' direction (Figure 3.8, right column) reproduce the experimental band structures well. Except for the spin-splitting the simulations with and without spin-orbit coupling show a similar distribution of photoemission intensity.

We now focus on the photoemission intensity from the top-most valence band. The sim-

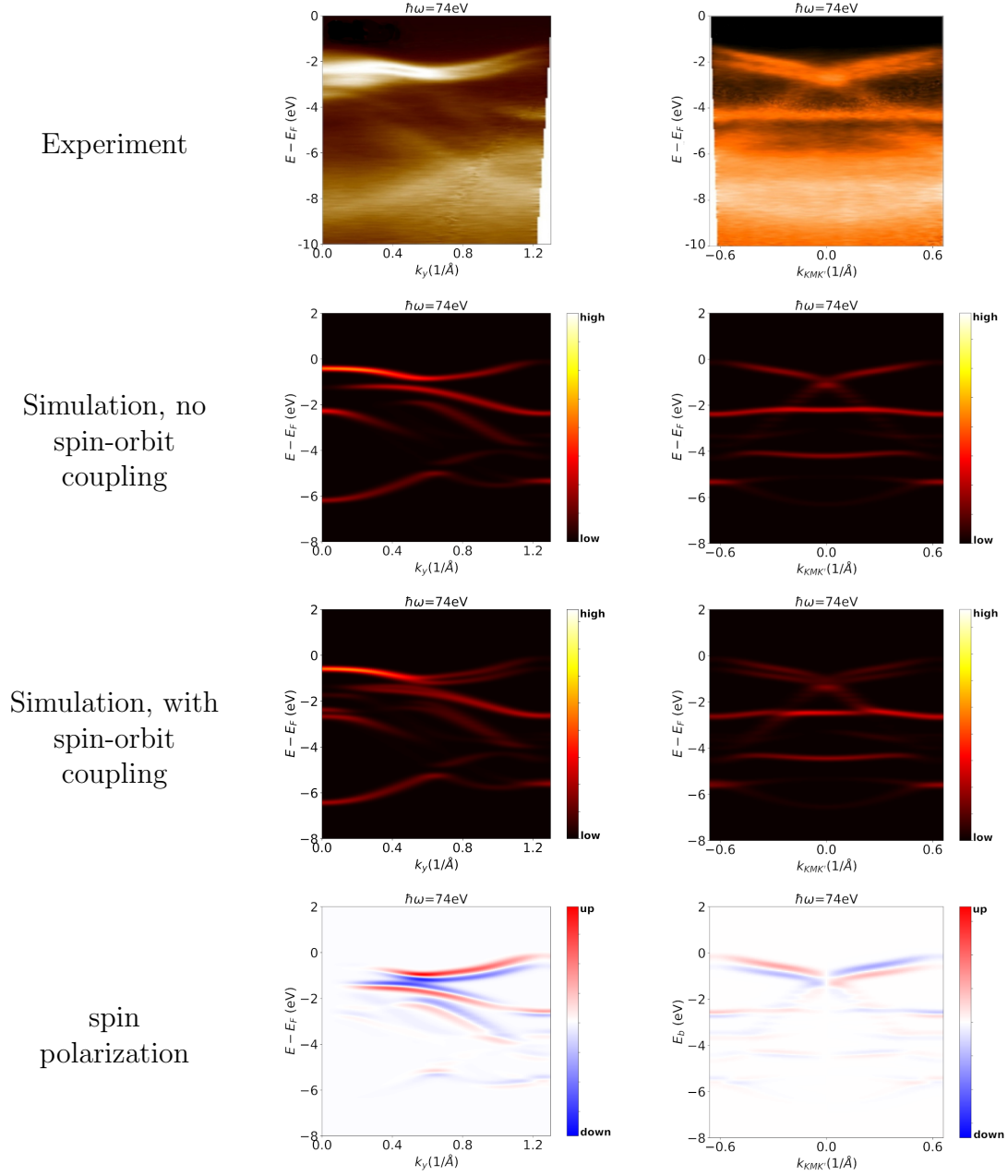


Figure 3.8: Band maps of WSe₂, photon-energy 74 eV; top row: Experiment taken from reference [43]; bottom row: simulations done as described in the text; left side: Γ -K direction, right side: K - M - K' direction

ulations and experiments are in good agreement. There is high intensity at the Γ -point and a minimum in intensity at the K -point. However, the simulated band maps in Γ - K direction somewhat deviate from the experimental maps regarding the lower lying bands (Figure 3.7, Figure 3.8 left column). In regions where in experiment a high intensity was

detected, the simulation shows a low intensity. For example at the Γ -point the second highest band is visible that does not show in the simulations. Additionally there is a crossing of bands at $k_y \approx 0.7 \text{\AA}^{-1}$ and $E_B \approx 6.5 \text{ eV}$ that is visible in the experiment but does not appear in the simulations (Figure 3.8 right side). In K - M - K' direction (Figure 3.8 left side) the simulation reproduces the photoemission from the highest three occupied bands that are visible, well. The bands measured in experiment at approximately 8 eV binding energy are missed by the simulations.

Inspection of Figure 3.7d and the bottom right panel of Figure 3.8 demonstrates that the signal from the top-valence band at the K -point is spin-polarized. This agrees with spin-resolved ARPES measurements that also reveal a similar polarization [39]. The simulation for the polarization in K - M - K' direction (Figure 3.8 bottom right) shows that the polarization changes sign when going from $+k$ to $-k$. Similar results are obtained from simulating ARPES using methods related to time dependent density functional theory [44] which also predicts a spin-polarized top-valence band at the K -point and a sign change in the polarization when going from $+k$ to $-k$.

In conclusion the simulations for WS_2 and WSe_2 are in good agreement with the experiments. Already the simulations without SOC already reproduce the measured ARPES-maps well. When including SOC, the resulting spin-splitting at the K -point improves the agreement of the simulations with the ARPES-band maps. Importantly, the spin-splitting also affects the bandgap WS_2 and WSe_2 .

When taking into account spin-orbit interactions in the simulations of ARPES-experiments the major changes are due to the altered band structure compared to the simulation without SOC. Furthermore, including SOC allows to simulated the spin-polarization of the ARPES signal. For the cases of WS_2 and WSe_2 , the simulated spin-polarization is in good agreement with experimental results and other calculations. To sum up, including SOC in ARPES-simulations does improve the agreement to experiments by improving the agreement of the electronic band structure to the band maps and introducing spin-polarization.

3.2 Monolayer of AgTe on Ag(111) Surface

To further test the ARPES-simulation for materials that show strong spin-orbit coupling, the electronic properties and ARPES maps of a monolayer silver-tellur (AgTe) on a $\text{Ag}(111)$ -surface are calculated. The simulations are then compared against experimental results taken from Reference [45].

Due to the broken inversion symmetry and a SOC, a spin-splitting of electronic bands can be observed. Some of these bands show a spin-splitting of the Rashba-type [45]. The Rashba effect causes an increase of the spin-splitting of two bands linearly depending on the momentum [46]. The aim of this section is to simulate the recorded ARPES maps and reproduce the spin-splitting and the distribution of photoemission intensity in the measured ARPES maps.

In the first part of this section, the geometric structure of surface is determined by

relaxing the atomic positions. Then the electronic bandstructure is calculated and its properties are analysed. Finally, ARPES-maps are simulated and compared against experimental data from Ref. [45].

3.2.1 Structure of AgTe/Ag(111)

The structure of the single layer AgTe on the Ag(111)-surface is set up as described in Ref. [45]. It is constructed from the surface of face-centered-cubic (fcc) bulk silver in (111) direction with a single layer of AgTe on top which forms a hexagonal honey-comb lattice. According to Ref. [45], the top-most layer forms a hexagonal-closed-packed (hcp) like stacking order where, the single layer AgTe is directly above the silver atoms of the underlying silver substrate. Expressed in the stacking order of an hcp-structure of the three top-most layers it would read: ...ABCA|C'. Where C' stands for the single layer of AgTe. To reduce computational costs, the bulk silver is modelled as a slab consisting of only 4 layers. The structure is set up as shown in Figure 3.9. The lattice constant of the structure is assumed to be equal to bulk silver, for which 4.152 \AA is used [47]. This is the equilibrium lattice constant for silver calculated with the PBE-GGA functional.

To obtain the relaxed structure, the atomic positions are optimized until all forces are smaller than 0.01 eV \AA^{-1} , where again the PBE-GGA functional is used. The first Brillouin zone was sampled using a $15 \times 15 \times 1$ grid in reciprocal space. Note that spin-orbit coupling has not been taken into account for the geometry relaxation.

Figure 3.9 shows the relaxed structure, where the grey spheres indicate silver atoms and yellow spheres tellurium atoms. Compared to the initial guess described above, the structure does not change significantly. Average atomic distances stay at 2.93 \AA , which are consistent with the used lattice constant of 4.152 \AA . The inter-layer distances ranging from 2.35 \AA to 2.39 \AA (Figure 3.9b) are also consistent with the structure of bulk silver. The adsorption height of the single layer AgTe of 2.35 \AA turns out to be equal

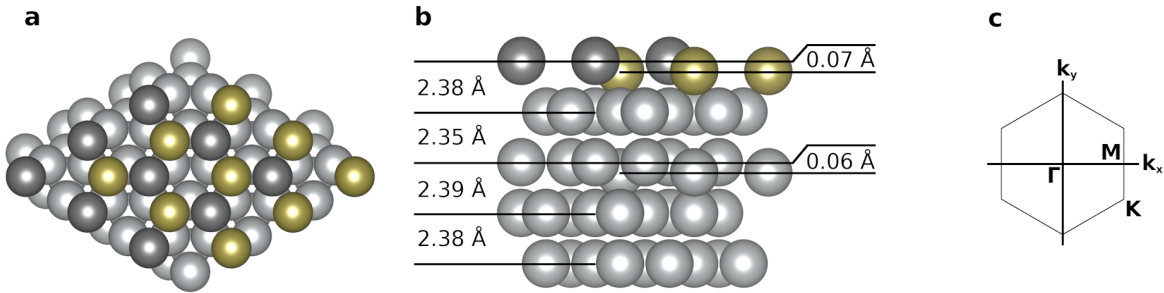


Figure 3.9: Relaxed structure of AgTe on a Ag(111) surface: (a) top-view; (b) side-view with interlayer distances (left) and height differences of single atoms (right); grey spheres: Ag atoms, dark grey spheres: Ag atoms in the surface layer, yellow spheres: Te atoms; (c) two dimensional Brillouin zone.

to the interlayer distance of bulk-silver. It should be noted that AgTe does not form an entirely flat layer, but the tellurium atoms are located 0.07 \AA beneath the silver atoms. This also influences the second to last layer of the bulk. The silver atoms directly below the tellurium atoms of the surface layer are pushed slightly downwards with respect to the other atoms of this layer. The structure obtained here conforms with the relaxed structure and STM measurements of Ref. [45].

3.2.2 Electronic Structure

In this section the band structure of AgTe on Ag(111) is calculated in two modes. First, without SOC, and second, with SOC included, in order to reveal the influence of SOC on the band structure and the simulated ARPES maps. Both types of calculations use a grid of $31 \times 31 \times 1$ points in momentum space to sample the first Brillouin zone.

In Figure 3.10a, the results of the band structure calculations are plotted. There, the continuous lines mark the band structure without SOC, whereas the dashed lines show the band structure calculated with SOC. Note that the bands of both calculations are plotted relative to the Fermi-energy of the calculation done without spin-orbit coupling. However, the Fermi energy rises by only 3 meV, when including SOC.

The most obvious difference between the calculations is that all bands in the region shown in Figure 3.10a obtain a spin-splitting. A change also occurs for the bands marked with α and β directly at the Γ -point. These two bands are degenerate at the Γ -point when no SOC is considered. Including spin-orbit interaction shifts the band-energies even at the Γ -point such that the degeneracy of the α - and β -bands are lifted. The latter result is supported by band maps measured using ARPES [45] (Figure 3.12a). Note that the states contributing to the corresponding bands are located in the surface layer of AgTe as can be seen in Figure 3.11a.

For the bands in the shown energy range a spin-splitting of the Rashba type occurs at the Γ -point [45, 46]. Typical for this effect is a linear dependence of the size of the splitting on the momentum. The calculated and experimental values of the splitting of the β -bands are plotted in Figures 3.10b,c. According to the calculation the linear dependence for these bands is valid only in the direct vicinity of the Γ -point $k \leq 0.05 \text{ \AA}^{-1}$ (Figure 3.10b). In the experiment the linear increase of the splitting is valid for $k \leq 0.15 \text{ \AA}^{-1}$. The calculation gives a slope of the size of the spin-splitting of approximately 1.7 eV \AA . This is slightly below the measured value of approximately 1.8 eV \AA (Figure 3.10c). This effect primarily occurs in the bands that are located in the surface layer consisting of the single layer of AgTe. Figure 3.11 shows the band structure projected onto the (s,p,d)-states of the atoms located in the surface layer. The size of the dots corresponds to how strongly the bands are located in the states of the surface-layer.

3.2.3 ARPES - Simulations

Similarly to the band structure calculation, also the simulations in this section are performed, both, without and with SOC, respectively. Results from the simulations are compared with each other and experimental data from Ref. [45]. A $29 \times 29 \times 6$ grid

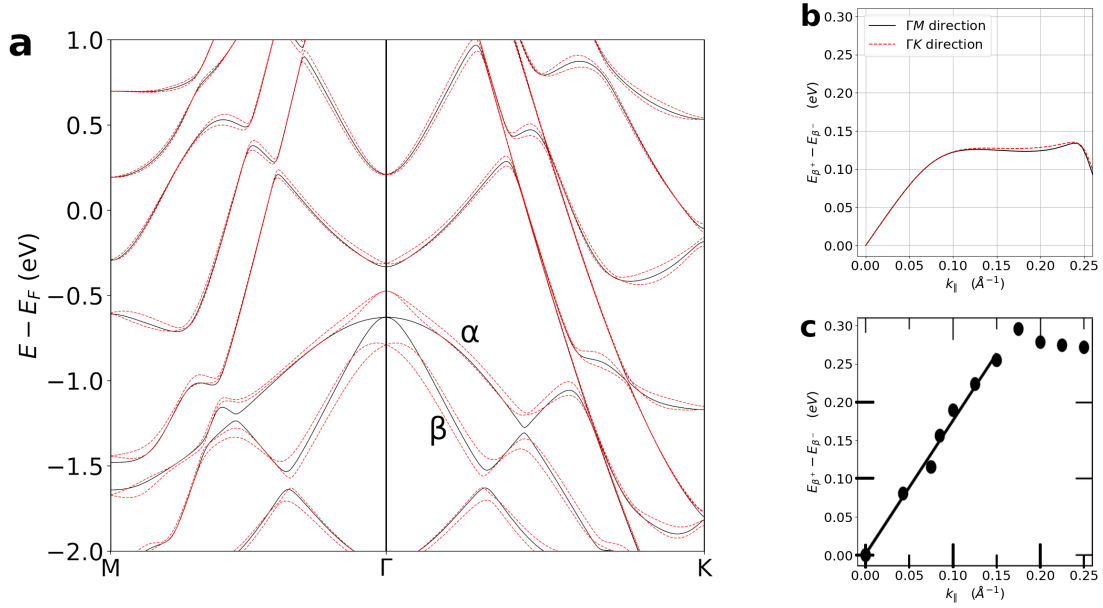


Figure 3.10: a: Electronic band structure AgTe on Ag(111); without SOC (full lines) and with SOC (dashed lines), the energies are aligned to the Fermi-level of the calculation without SOC; b,c: spin-splitting of the β -bands, b: calculation, c: experimental data Ref. [45].

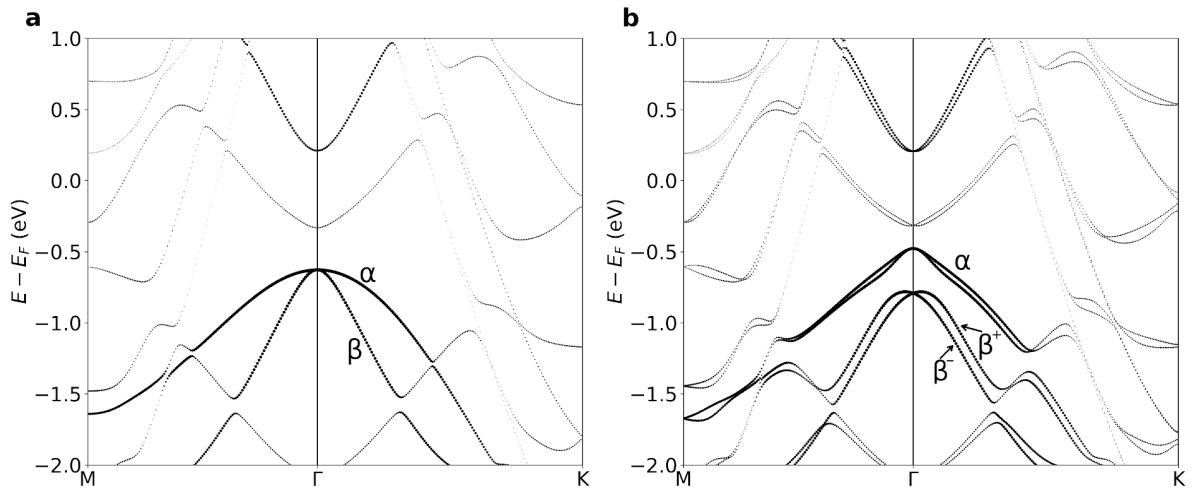


Figure 3.11: Band structure of AgTe on Ag(111) projected on the states in the AgTe layer; a: calculation without spin-orbit coupling; b: calculation with spin-orbit included; the size of the dots indicates the contribution of the states located in the top-most layer to the respective bands.

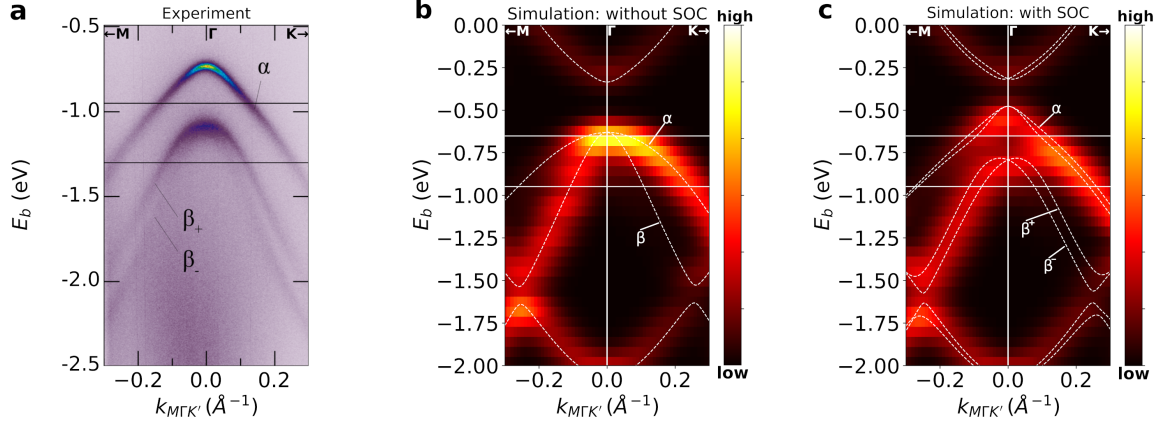


Figure 3.12: Band maps of AgTe on Ag(111) for a photon energy of 21.21 eV; a: measured band map along M- Γ -K [45]; b: simulated maps without spin-orbit interaction; c: simulated maps with spin-orbit interaction. The white dashed lines mark the band structure.

in momentum space is used for sampling the first Brillouin for the DFT calculation used as a basis for the ARPES-simulation. This gives a maximum resolution in momentum space of roughly 0.05 \AA^{-1} . Note that this resolution is, however, insufficient to reproduce finer details of the ARPES maps. Due to the high memory demand of the DFT calculation including SOC, the k -point sampling could not be increased further. All ARPES-intensity maps in this section are simulated using damped plane waves to describe the final states of the photoelectrons, where the signal originating from below the top layer is damped by a damping factor of 0.5 \AA^{-1} .

First, band maps are presented, where a photon-energy of 21.21 eV [45] consistent with the experimental value has been used. Figure 3.12a shows an ARPES band map measured in an experiment [45]. Here, the left half of the band map ($k_{\parallel} = -0.3 \text{ \AA}^{-1}$ through 0.0 \AA^{-1}) shows the Γ - M direction in reciprocal space, whereas, the right half ($k_{\parallel} = 0.0 \text{ \AA}^{-1}$ through 0.3 \AA^{-1}) shows the Γ - K direction. In Figures 3.12b,c correspondingly simulated band maps are shown, without and with SOC, respectively.

Due to the limited resolution only few details are discernible in the simulated maps. The β -bands, that can be clearly distinguished in the experiment (Figure 3.14a), appear as one band in the simulation (Figure 3.12c), although the spin-splitting of the β^+ - and β^- -bands is reproduced well by the calculations (Figure 3.10a). When including spin-orbit coupling the simulation (Figure 3.12c) shows a region of lower photoemission intensity between the α - and β -bands. But the two bands can not be as well differentiated as in the experimental map Figure 3.12a, due to the limited resolution.

In addition to the α - and β -bands, that constitute of states located in the top-most layer, also bands of the bulk silver contribute to the simulated band maps. The bands

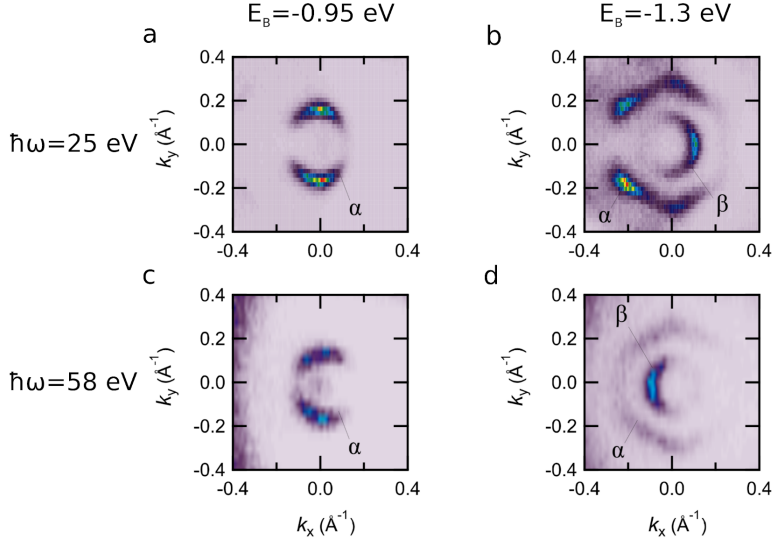


Figure 3.13: Measured momentum maps of AgTe on Silver (111) [45]; a,b: photonenergy 25 eV; c,d: photonenergy 58 eV; a,c: binding energy -0.95 eV; b,d: binding energy -1.3 eV; the binding energies are marked in Figure 3.12a

appearing directly below and above the α - and β -bands originate mainly from state located in the bulk (projected band structure: Figure 3.11). These bands do not seem to appear in the experiments. A reason for them appearing in the simulation might be, that too few layers of the bulk were included in the DFT calculation since including additional layers shifts the electronic bands in the bulk.

Regarding the observed maximum of the photoemission intensity around the Γ -point, the simulated band maps are in agreement with the experimental maps. In both directions (Γ - K , Γ - M) the simulations predict emissions from the α - or β -bands to be more intense, where the bands emitting higher intensity changes depending on the direction. There, both simulations agree with each other. However, neither of the simulations agrees with the observed trend, that all bands (α , β^+ , β^-) contribute equally to the emitted intensity. At a binding energy of around -1.5 eV, both simulations show a crossing of the bands located in the surface layer and the bulk. These crossings do not appear in the experiment.

In summary it must be concluded that the simulate band maps do not agree with the measured ones regarding the intensity distribution and the precise shape of the band structure. Only in the vicinity of the Γ -point ($k_{\parallel} \leq \sim 0.1 \text{ \AA}^{-1}$) can the simulations reproduce the experiment. But for details in this region the resolution of the simulated maps is too low.

In the second part of this section simulated momentum maps at selected binding-energies are compared to available experimental data (Figure 3.13). Two different photon-energies were used (25 eV: Figure 3.13a,b; 58 eV: Figure 3.13c,d). For each photon-

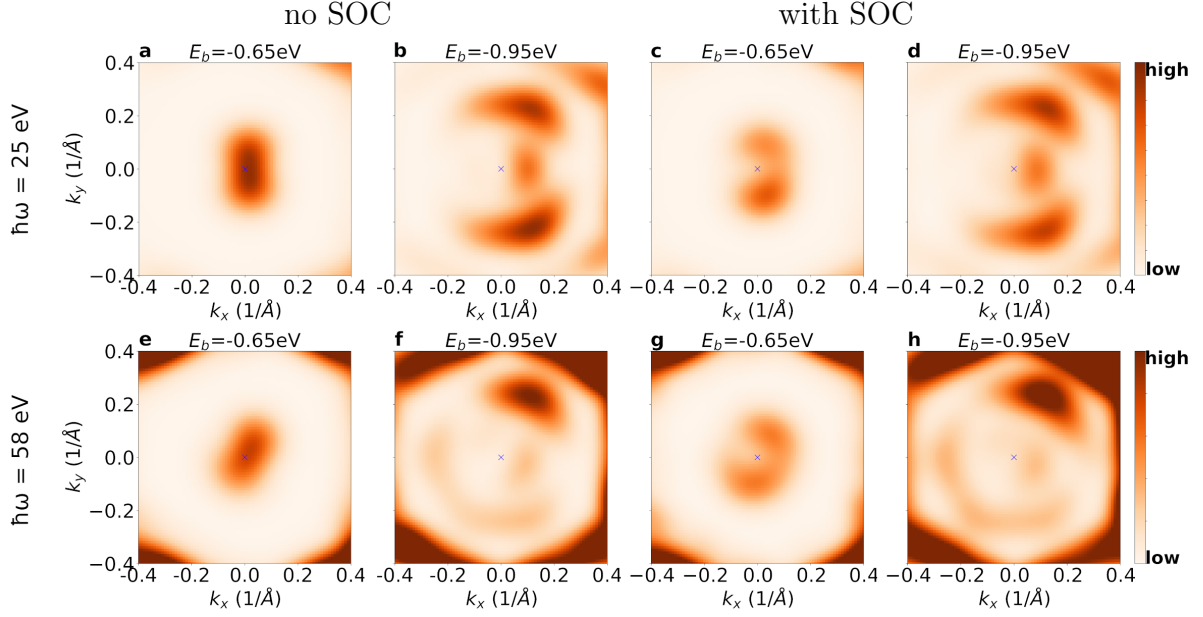


Figure 3.14: Simulated momentum maps of AgTe/Ag(111); a-d: photon-energy 25 eV; e-h: photon-energy 58 eV; a,e,c,g: binding-energy -0.65 eV; b,f,d,h: binding-energy -0.95 eV, the binding energies are marked in Figures 3.12b,c; without SOC: a,b,e,f; with SOC : c,d,g,h

energy used, two maps at different binding energies (-0.95 eV: Figure 3.13a,c; -1.3 eV: Figure 3.13b,d) are shown. In the vicinity of the Γ -point the maps show cuts through the α - and β -bands of the band structure Figure 3.10a. Remarkable is that only partial rings are formed around the Γ -point due to the orbital angular momentum of the states involved [45]. Since different states with different orbital angular momentum are involved in the α - and β -bands visible in the momentum maps for a binding energy of -1.3 eV, the visible parts of the rings change.

The simulated momentum maps corresponding to the maps in Figure 3.13 are shown in Figure 3.14. The upper row shows simulations for a photon-energy of 25 eV (Figure 3.14a-d), the lower row for a photon-energy of 58 eV (Figure 3.14e-h). The first and second column show simulations without SOC (Figure 3.14a,b,e,f), while the simulations in the third and fourth column are with SOC (Figure 3.14c,d,g,h). The simulations in the first and third column are done for a binding energy of -0.65 eV (Figure 3.14a,e,c,g) and the second and fourth column are done for a binding energy of -0.95 eV (Figure 3.14c,d,g,h). Compared to the experiment the binding energies are adjusted by a shift of 0.3 eV to fit to the calculated band structure.

Simulations for a photon-energy of 25 eV agree well with the experiment. The simulations show partial rings around the Γ -point. At a binding energy of -0.65 eV the parts of the rings that are visible are parallel to the k_x -axis in reciprocal space. Here, only contributions from the α -bands are visible. At an increased binding energy of -0.95 eV the β^+ - and β^- -bands also emit electrons that are visible near the Γ -point. The contribution

from the β -bands have an intensity maximum on one side of the Γ -point perpendicular to the k_x -axis. The simulations calculated with and without spin-orbit coupling show similar results. Both reproduce the experimental results. To see the influence of spin-orbit coupling on the momentum maps the resolution in momentum space is too low. When going to a higher photon-energy of 58 eV, the experimental signatures do not change significantly. The bands again form ring-like structures around the Γ -point. Where the α -bands form structures parallel to the k_x -axis in momentum space and the β -bands perpendicular to the k_x -axis. However, the simulations indicate, that the pattern of the distribution of the emitted intensity gets tilted by around 45° , both simulations, with and without spin-orbit coupling, show the same results. In this way the simulated and measured maps are not in agreement. The shown area of the simulations is surrounded by areas of high intensity. This emitted intensity originates from electronic states in the bulk (Figure 3.11).

In conclusion, the simulated ARPES intensity maps do not reproduce the experimental data well. For the lower photon-energy of 25 eV the simulated photoemission intensity from the α - and β -bands are in agreement with the experimental maps. However, for the higher photon-energy of 58 eV the simulated intensity distributions do not agree with the experiments. Additionally, simulations for both photon-energies show contributions from bands of the bulk silver that are absent in the experimental data.

The additional bands in the simulated maps might be due to using too few layers to simulate the bulk silver. Using additional layers might shift the bands of the bulk which would remove their contributions to ARPES maps in the considered range of binding energies.

Regarding the intensity distribution of the α - and β -bands. The differences between simulations and experiment might be due to the shortcomings of the plane wave final states. In the first place, the plane wave final state approach works best for organic molecules containing light elements like carbon and oxygen [13]. Additionally, plane waves are not suited for mapping angular distributions and representing states with angular momentum. However, the intensity distribution in the experiment is mainly due to the orbital angular momentum of the states involved [45]. Thus, the differences between the simulation and experiment might be due to an inappropriate description of the final states used in the description of the photoemission process.

The resolution of the simulation is too low to resolve the spin-split bands. This spin-splitting is expected from the experimental maps and the band structure calculations.

3.3 Tight Binding Simulation for Graphene

In this section, ARPES maps for single layer graphene and bilayers of graphene are simulated using a tight binding model as implemented in the python package *chinook* [12]. Based on a tight binding (TB) model for the electronic band structure, *chinook* simulates ARPES maps by expanding the plane wave final state of the photoelectrons in a Rayleigh expansion as described in Section 2.4.3. To test, whether *chinook* gives

reliable results, ARPES-maps are simulated with *chinook* and the PWFS approach based on DFT calculations (DFT+PWFS) as described in Section 2.4.1. The maps are then compared to show whether the maps calculated using *chinook* show different features. The systems that are used for this test are single-layer graphene (SLG) and bilayer graphene (BLG) in AA (BLG-AA) and AB (BLG-AB) stacking order, respectively. For all three cases, the corresponding TB model is fitted to the band structure obtained from a DFT calculation. For the TB models of the three systems only of p_z orbitals have been considered. The fit of the TB-bands to the DFT-bands is done using the method of simulated annealing [48] by varying the parameters of the TB model. During the fitting process, the square of the energy difference between the TB-bands ($E_n^{TB}(\vec{k})$) and the DFT-bands ($E_n^{DFT}(\vec{k})$) is minimized:

$$(\Delta E)^2 = \sum_{n, \vec{k}} (E_n^{DFT}(\vec{k}) - E_n^{TB}(\vec{k}))^2 \longrightarrow \min \quad (3.1)$$

The first part of this section deals with the results for SLG, while the second and third parts treat BLG-AA and BLG-AB respectively. Each part contains a description of the TB model and simulations of ARPES-maps. A short description of the usage of *chinook* can be found in the Appendix: usage of *chinook*.

3.3.1 Single Layer Graphene (SLG)

DFT Calculation for SLG

Graphene forms a flat 2-dimensional hexagonal lattice of carbon atoms as shown in Figure 3.15a. The lattice constant of 2.47 Å is obtained from a geometry relaxation. For the band structure calculation a $81 \times 81 \times 1$ grid is used to sample the first Brillouin zone with a plane-wave cut-off of 450 eV. The treatment of the exchange-correlation energy is done using the PPE-GGA functional.

Tight-binding Model for SLG

To calculate the TB model one p_z orbital is used per carbon atom on the sites A and B. Using only p_z orbitals is possible since the bands near the Fermi-level are composed of those orbitals. Restricting the model to include only nearest neighbour hopping, the Hamilton matrix can be written as [31]

$$H = \begin{matrix} & \begin{matrix} A & B \end{matrix} \\ \begin{matrix} A \\ B \end{matrix} & \begin{pmatrix} \epsilon & -t \\ -t & \epsilon \end{pmatrix} \end{matrix}, \quad (3.2)$$

where the diagonal elements ϵ stand for the orbital energy of the p_z orbitals on the different atoms and t is the hopping integral between the p_z orbitals on the inequivalent carbon atoms A and B. The diagonal elements are set to $\epsilon = 0$ eV as they only cause an energy shift. The hopping parameters t are obtained from the fit to the DFT band

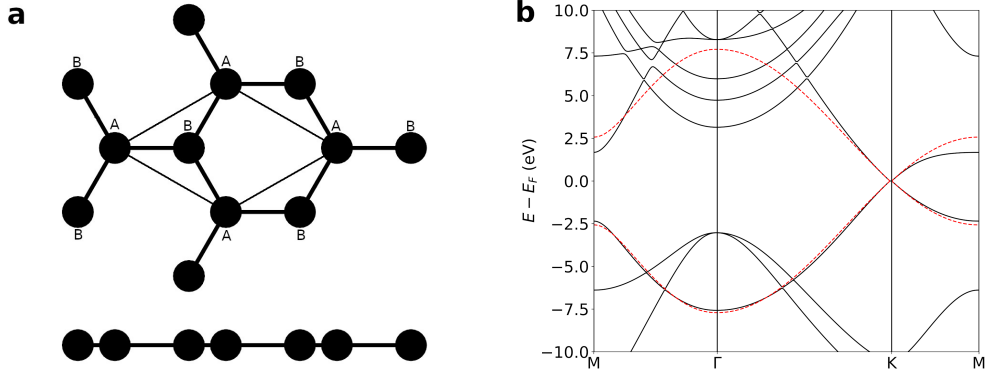


Figure 3.15: a: Structure of single-layer graphene in top-view (top) and side-view (bottom); b: Electronic band structure of SLG, full lines: DFT calculation, dashed lines: TB calculation

structure (Figure 3.15b) which results in $t = 2.56 \pm 0.01$ eV. The k -dependence of eigenvalues is calculated numerically as described in Section 2.3.

Figure 3.15b shows the DFT band structure (full lines) together with the fitted TB band structure (dashed lines). Around the K -point both band structures show the linear dispersion that is typical for graphene. The TB band structure is able to reproduce the DFT band structure there. The unoccupied band of the TB-model does not fit so well to the DFT-calculation because the overlap matrix has been neglected in the TB model. As a result, the TB band structure is symmetric around the Fermi-level. Nevertheless, the occupied band is in good agreement with the DFT-band structure, which is essential for the ARPES-simulation.

ARPES simulations for SLG

The ARPES simulations for this section are calculated for a photon energy of 40 eV. The simulation using the DFT+PWFS approach is based on a DFT calculation that samples the first Brillouin zone using a $79 \times 79 \times 16$ grid in reciprocal space. This results in a resolution of 0.04 \AA^{-1} of the simulated maps. The parameters *chinook* uses for the ARPES simulations are adjusted to give the same resolution. Both simulations use a workfunction of 4.282 eV, as obtained from the DFT-calculation. The polarization is in the DFT+PWFS approach with an angle of incidence of 90° , which corresponds to a linear polarization in z -direction in *chinook*.

Figure 3.16 shows the simulated momentum maps for SLG. The upper row shows simulations done using *chinook*, the lower row contains the maps simulated using the DFT+PWFS approach. The ARPES momentum maps simulated using both methods agree with each other as far as the TB-model can reproduce the respective electronic bands. Both methods show the Dirac cones at the K -points at the corners of the first Brillouin zone. For lower binding energies the points open to pockets that are open to the

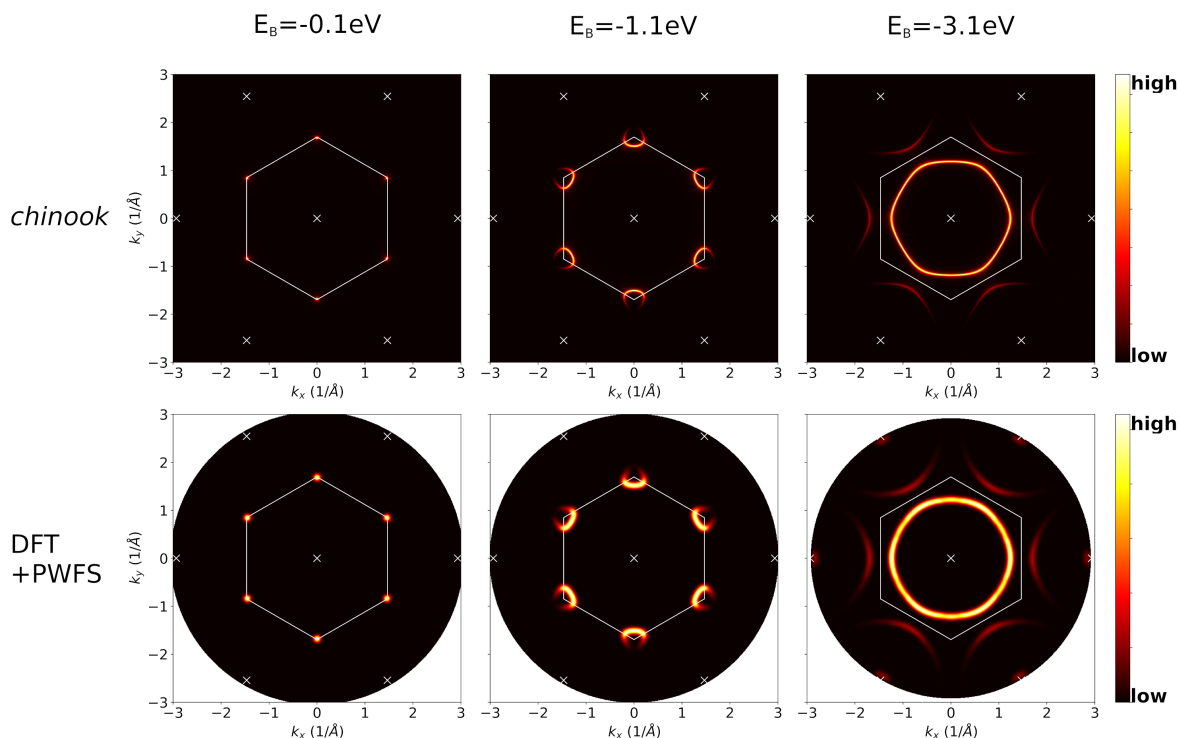


Figure 3.16: SLG: ARPES momentum maps; photon energy: 40 eV; top row: maps simulated using *chinook*; bottom row: simulations using DFT+PWFS approach; lines inset: boundary of the first Brillouin zone, crosses: Γ -points

outside of the Brillouin zone. The direction where the circles open depends for the tight-binding model on the sign of the hopping parameter t in the Hamilton matrix (Equation 3.2). When changing the sign of t the direction where the circles open changes, since changing the sign of the hopping term interchanges valence and conduction bands [49]. However, the TB band structure does not change. The sign used before, is the correct one.

At approximately -3 eV binding energy the PWFS simulation show emissions from σ -bands that are visible at the Γ points outside the first Brillouin zone (bright spots at the border of the visible area). These emissions are clearly absent in *chinook*, since only π -bands are included in the model.

The simulated band maps (Figure 3.16) show similar results. The contributions of the π -bands are the same for both the simulations. Contributions from the σ -bands are again missing in the TB-model.

In Figure 3.18 the photoelectron intensity is plotted against the photon energy $\hbar\omega$. This intensity is measured for an initial state close to the Dirac point at a binding energy of -0.1 eV. The signal is averaged and normalized to one for the peak in photoemission intensity for each calculation separately. The curves are calculated for *chinook* (red dashed line) and DFT+PWFS (black continuous line). To take into account the the

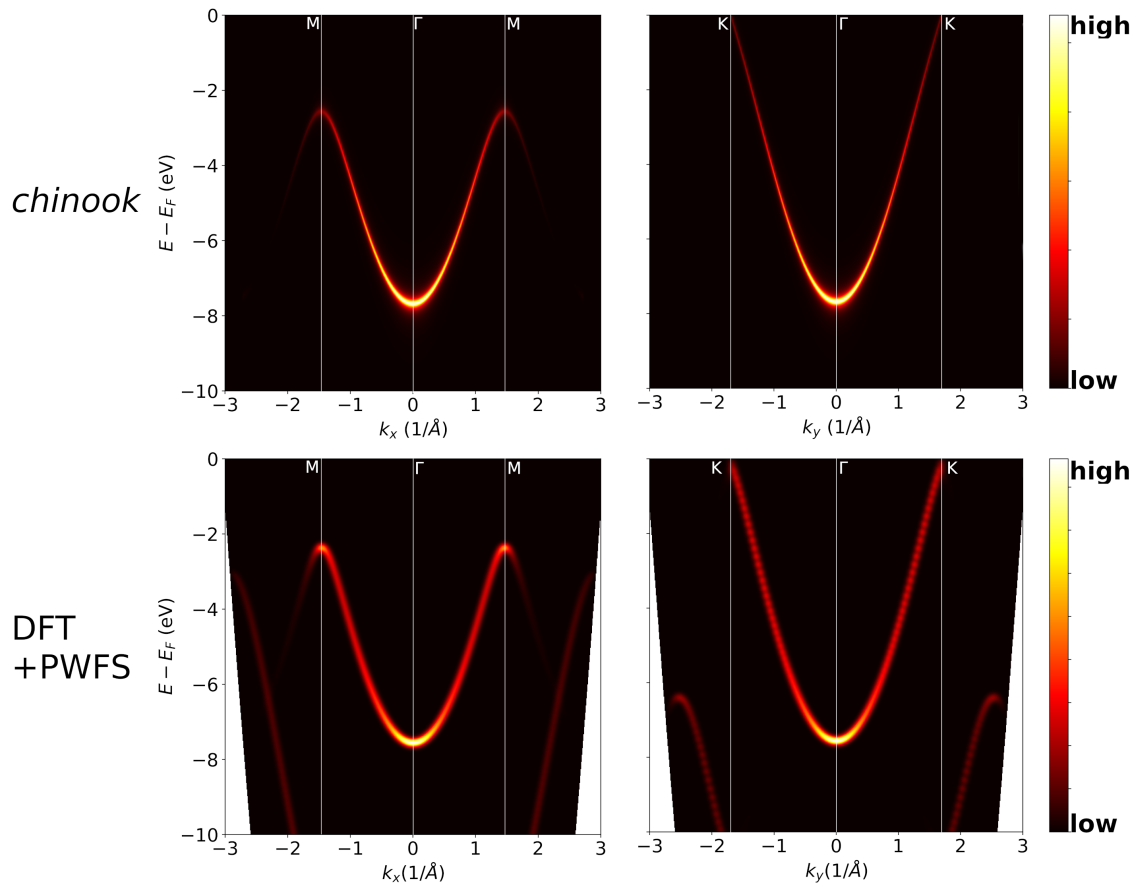


Figure 3.17: SLG: ARPES band maps; photon energy: 40 eV; left panels: maps simulated using *chinook*; right panels: simulations using the DFT+PWFS approach

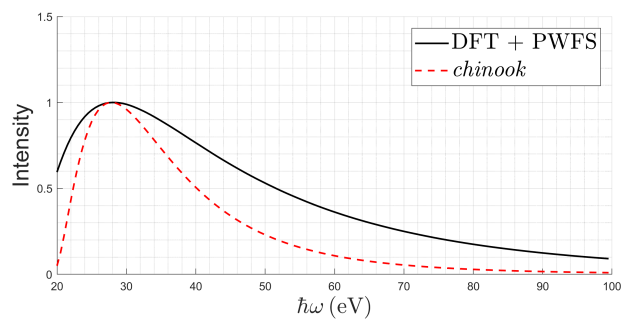


Figure 3.18: SLG: photoemission intensity versus photon energy, measured for initial states $E_B = 0.1$ eV around one K -point ($1.48 \text{ \AA} \leq k_{\parallel} \leq 1.89 \text{ \AA}$)

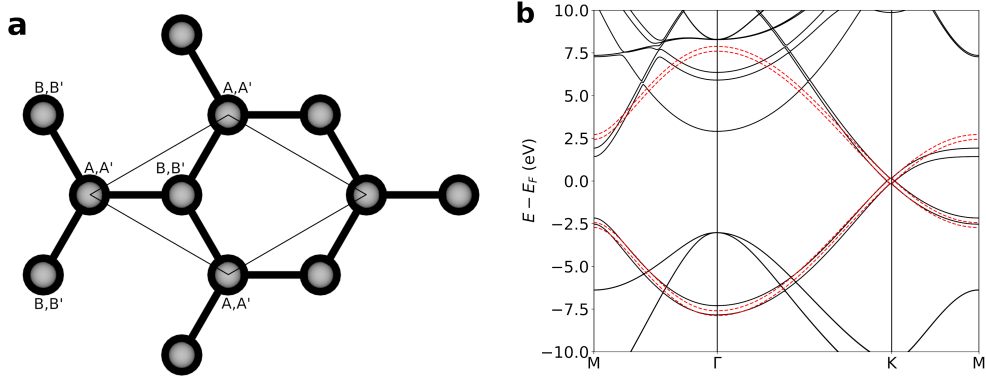


Figure 3.19: a: Structure of BLG-AA top-view, grey spheres: carbon atoms in the top sublayer, black spheres: carbon atoms in the bottom sublayer; b: electronic band structure of BLG-AA, full lines: DFT calculation, dashed lines: TB model

dependence of the vector potential on the photon energy $\hbar\omega$, a factor of $\frac{1}{\hbar\omega}$ is included in the DFT+PWFS approach.

Both simulations show one maximum of the emitted photoelectrons at a photon energy of 28 eV. To higher photon energies the intensity is decaying slowly, where the curve calculated for *chinook* is decaying faster. The form of the photon energy dependence conforms with the Fourier transform of the p_z orbital, which is the analytic form of the energy dependence [50].

3.3.2 Bilayer Graphene in AA Stacking Order (BLG-AA)

DFT Calculation for BLG-AA

The structure of BLG-AA is formed of two sublayers of graphene, where each atom in the top layer is located above an atom in the bottom layer. Figure 3.19a shows the top view of the structure. Carbon atoms in the top layer are coloured in grey and the atoms in the bottom layer in black. The lattice constant of 2.47 Å of single layer graphene is also used for the simulations of the bilayer graphene. For the distance between the sublayers a value of 3.76 Å is used, which has been obtained from a structure relaxation, where the intra-layer distances were kept fixed. For the band structure calculation a $81 \times 81 \times 1$ grid is used to sample the first Brillouin zone with a plane-wave cut-off of 450 eV. The treatment of the exchange-correlation energy is done using the PPE-GGA functional. van der Waals interactions are treated using the DFT-D3 method [51].

Tight-binding Model for BLG-AA

For setting up the TB-model one p_z orbital is placed on each carbon atom, where A, B are located in the bottom sublayer and A', B' are located in the top sublayer. Again the

model includes only nearest neighbour interactions. Hopping is possible inside the layer (t_1) where the hopping constant is the same for both sublayers. Between the layers only the contributions from the atoms above each other are considered (t_2). The Hamilton matrix can then be written [2]:

$$H = \begin{matrix} & A & B & A' & B' \\ \begin{matrix} A \\ B \\ A' \\ B' \end{matrix} & \begin{pmatrix} \epsilon_1 & -t_1 & t_2 & 0 \\ -t_1 & \epsilon_1 & 0 & t_2 \\ t_2 & 0 & \epsilon_2 & -t_1 \\ 0 & t_2 & -t_1 & \epsilon_2 \end{pmatrix} \end{matrix} \quad (3.3)$$

The Hamiltonian splits into the contribution from intra-layer hopping of the two sublayers on the diagonal blocks. ϵ_1 and ϵ_2 are the orbital energies of the p_z orbitals in the different layers which are set to $\epsilon_1 = \epsilon_2 = 0$ since the layers are symmetric. The hopping parameter t_2 on the off-diagonal blocks accounts for the inter-layer hopping. From the fit of the tight binding band structure to the DFT-band structure the parameters are determined as: $t_1 = 2.58 \pm 0.01$ eV and $t_2 = 0.18 \pm 0.01$ eV.

In Figure 3.19b the DFT- (full line) and the TB- (dashed line) band structures are plotted. Similar to the case for the SLG, the band structures agree best around the K -point. The TB model is able to reproduce the same splitting of the bands at this point. This splitting is not the same over the whole band structure. Near Γ the TB model underestimates the splitting of the bands. Regarding the unoccupied bands the TB model deviates from the DFT results more strongly for the same reason as for SLG. Overall the π -bands of the two calculation methods are in good agreement. By construction, the TB-model does not include the deeper lying σ -bands.

ARPES Simulations for BLG-AA

The simulation of the ARPES-maps for BLG-AA is done using the same parameters as for the single layer graphene. This means a photon energy of 40 eV and a resolution of less than 0.04 \AA^{-1} . Both simulations use a work-function of 4.275 eV, as obtained from the DFT-calculation. The polarization is in the DFT+PWFS approach with an angle of incidence of 90° , which corresponds to a linear polarization in z -direction in *chinook*. Figure 3.20 shows the simulated momentum maps. The upper row of the figure shows simulations done using *chinook*, whereas the lower row contains the simulated maps of the DFT+PWFS approach. Similar to the case of SLG, both simulations show almost the same results. Differences are mainly due to the slightly different band structures and the missing σ -bands not included in the TB-model. Both simulations show almost the same structure of the pockets around the K -points that are open to the outside of the first Brillouin zone. The pockets, in fact, get contributions from two separate bands, where in the momentum maps (Figure 3.20) the inner-lying bands show a larger contribution to the photoemission intensity. These different contributions can be well seen in the band maps in Figure 3.21. When simulating the maps using *chinook* the relative intensities of these bands depend on the sign of the inter-layer hopping constant t_2 (Equation 3.3), where the sign used in the previous section is the correct one. If t_2

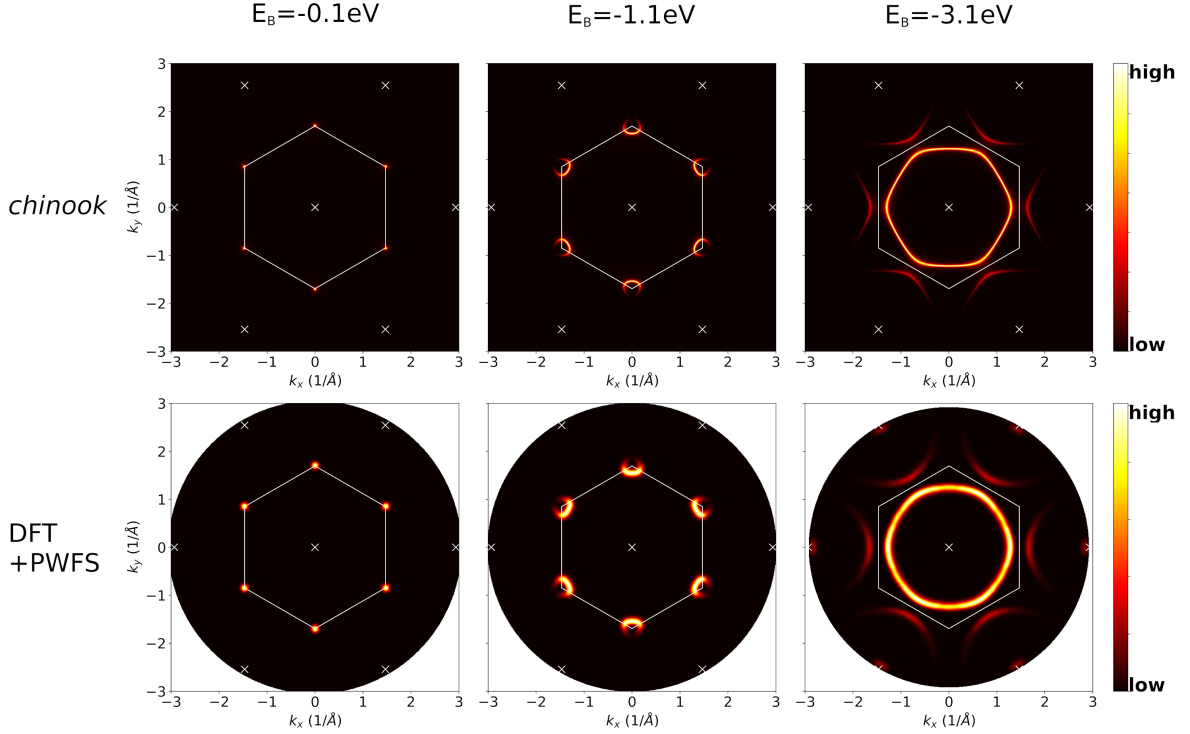


Figure 3.20: BLG-AA: ARPES momentum maps: photon energy 40 eV; top row: maps simulated using *chinook*; bottom row: simulations using the DFT+PWFS approach; lines inset: boundary of the first Brillouin zone, crosses: Γ -points

has an additional minus sign, the band giving the larger contribution changes. The band maps simulated for this system are plotted in Figure 3.21, where the simulations are done for the ΓK -direction. Figure 3.21a shows simulations of *chinook* and Figure 3.21b contains the simulation using the DFT+PWFS approach. Regarding the π -bands the simulations of both methods are in good agreement, except for the σ -band emissions that are missing. In Figure 3.21b these contributions are visible at higher momenta. At Γ the splitting of the bands is clearly visible. As discussed before, the bands show different contributions to the photoemission intensity, where the upper band contributes less. The upper band in the band maps corresponds to the outer-lying band of the pockets in the momentum maps (Figure 3.20). Both simulations agree on the distribution of intensity between the bands. *chinook* underestimates the splitting of the bands as already follows from the band structures in Figure 3.19b. Figure 3.22 compares the dependence of the photoemission intensity on the photon energy $\hbar\omega$ for both methods. The photoemission intensity is measured for an initial state binding energy of -0.1 eV in the vicinity of the K -point. The signal is averaged over this region. The maxima of the curves at around 28 eV are normalized to one. Again, as for SLG, a factor of $\frac{1}{\hbar\omega}$ is included in the DFT+PWFS approach. Both calculations show a maximum of emission at similar photon energy (DFT+PWFS:

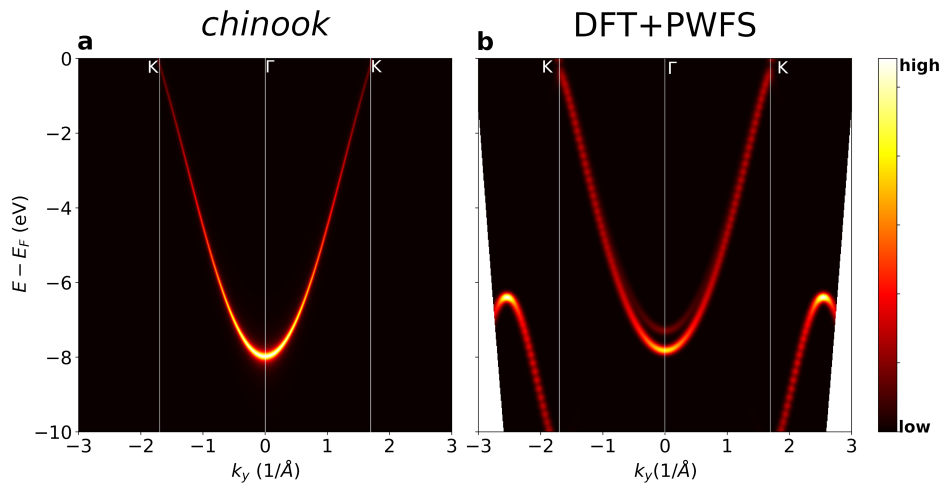


Figure 3.21: BLG-AA: ARPES band maps in ΓK -direction, photon energy 40 eV; a: simulation using *chinook*; b: simulation using the DFT+PWFS approach

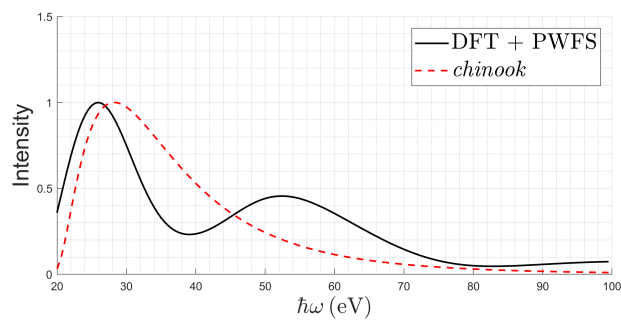


Figure 3.22: BLG-AA: photoemission intensity versus photon energy, measured for initial states $E_B = 0.1$ eV around one K -point ($1.48 \text{ \AA} \leq k_{\parallel} \leq 1.89 \text{ \AA}$)

26 eV, *chinook*: 28 eV). The results of *chinook* for BLG-AA show the same dependence as for SLG. In contrast, the DFT+PWFS calculation shows a minimum at 39 eV and an additional maximum at 52 eV. At higher photon-energies there possibly are further minima and maxima. Thus the dependence of the photoemission intensity calculated for the two methods do not agree.

For bilayers graphene, it is expected that the photoemission shows oscillations depending on the photon energy respectively depending on k_{\perp} for constant k_{\parallel} . Ref. [2] reports such oscillations for multi-layers of graphene with maxima in the photoemission. For BLG the maxima are located at $k_{\perp} \approx 4.0 \text{ \AA}^{-1}$ and $k_{\perp} \approx 5.0 \text{ \AA}^{-1}$, which corresponds to an energy-difference of approximately 28 eV. This value fits well to the difference between the maxima of the DFT+PWFS simulation of 26 eV.

3.3.3 Bilayer Graphene in AB Stacking Order (BLG-AB)

DFT Calculation for BLG-AB

The structure of BLG-AB is formed of two separate sublayers of graphene. But compared to the structure of BLG-AA discussed in the previous section, one layer is shifted by half a lattice vector of graphene. Figure 3.23a shows the top-view of the resulting structure. There the carbon atoms of the top layer are coloured grey and the atoms in the bottom layer are coloured black. The lattice constant of 2.47 Å of SLG is used. For the distance of the sublayers the value of 3.56 Å is used, which has been obtained from a structure relaxation, where the intra-layer distances were kept fixed. For the band structure calculation a $81 \times 81 \times 1$ grid is used to sample the first Brillouin zone with a plane-wave cut-off of 450 eV. The treatment of the exchange-correlation energy is done using the PPE-GGA functional. van der Waals interactions are treated using the DFT-D3 method [51].

Tight-binding Model for BLG-AB

As in the previous sections on BLG-AA, for the TB model one p_z orbital is placed on each carbon atom. The first (A) and the fourth (B') orbital of the model are on the atoms directly above each other (e.g. the site in the center of Figure 3.23a). Interlayer hopping (t_2) is only possible between these sites, since only nearest neighbour interactions are considered. The intra-layer hopping has again the form of SLG (Equation 3.2). From this one can write the Hamilton matrix:

$$H = \begin{matrix} & A & B & A' & B' \\ \begin{matrix} A \\ B \\ A' \\ B' \end{matrix} & \begin{pmatrix} \epsilon & -t_1 & 0 & t_2 \\ -t_1 & \epsilon & 0 & 0 \\ 0 & 0 & \epsilon & -t_1 \\ t_2 & 0 & -t_1 & \epsilon \end{pmatrix} \end{matrix} \quad (3.4)$$

As in the previous section, the Hamiltonian splits into contributions of intra-layer hopping in the blocks along the diagonal and the contribution of inter-layer hopping on the

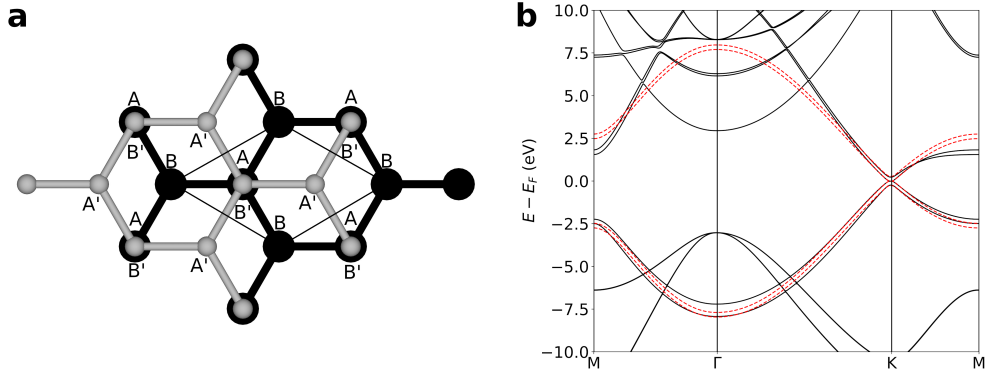


Figure 3.23: a: Structure of BLG-AB in topview, grey spheres: carbon atoms in the top sublayer, black spheres: carbon atoms in the bottom sublayer; b: electronic band structure of BLG-AB, black continuous line: DFT calculation, red dashed line: TB calculation

off-diagonal blocks. The on-site energy ϵ and the hopping term t_1 describe hopping in the graphene sublayers. t_2 describes hopping between the layers. The on-site energies are set to $\epsilon = 0$ eV. The other parameters are again obtained from a fit to a DFT band structure as follows: $t_1 = 2.61 \pm 0.01$ eV and $t_2 = 0.27 \pm 0.01$ eV.

Figure 3.23b gives the band structure of BLG-AB calculated using DFT (full lines) and the TB model described above (dashed lines). Similar to the calculations described in the previous sections, the TB model reproduces the DFT band structure best near the K -point. Both calculations show that the bands do not cross at the K -point but only touch. The occupied bands show an energy splitting that is reproduced correctly near the K -point by the TB model. When going to Γ the energy splitting is underestimated by the TB model. The unoccupied bands again do not agree with the DFT-calculation and only the π -bands appear in the TB-band structure since only those are considered in the TB model for BLG-AB. Considering the TB model, the calculated band structures are in good agreement.

ARPES Simulations for BLG-AB

The simulations of ARPES maps for BLG-AB are done using the same parameters as in the simulations of the previous sections on graphene. This means a photon energy of 40 eV and a resolution in momentum space of 0.4 \AA . Both simulations use a work-function of 4.289 eV, as obtained from the DFT-calculation. The polarization is in the DFT+PWFS approach with an angle of incidence of 90° , which corresponds to a linear polarization in z -direction in *chinook*.

Similar to the previous sections about graphene, the simulations done using the two methods are in good agreement regarding the π -bands. The main differences stem from the TB model that only includes p_z orbitals. Furthermore the model does not capture all

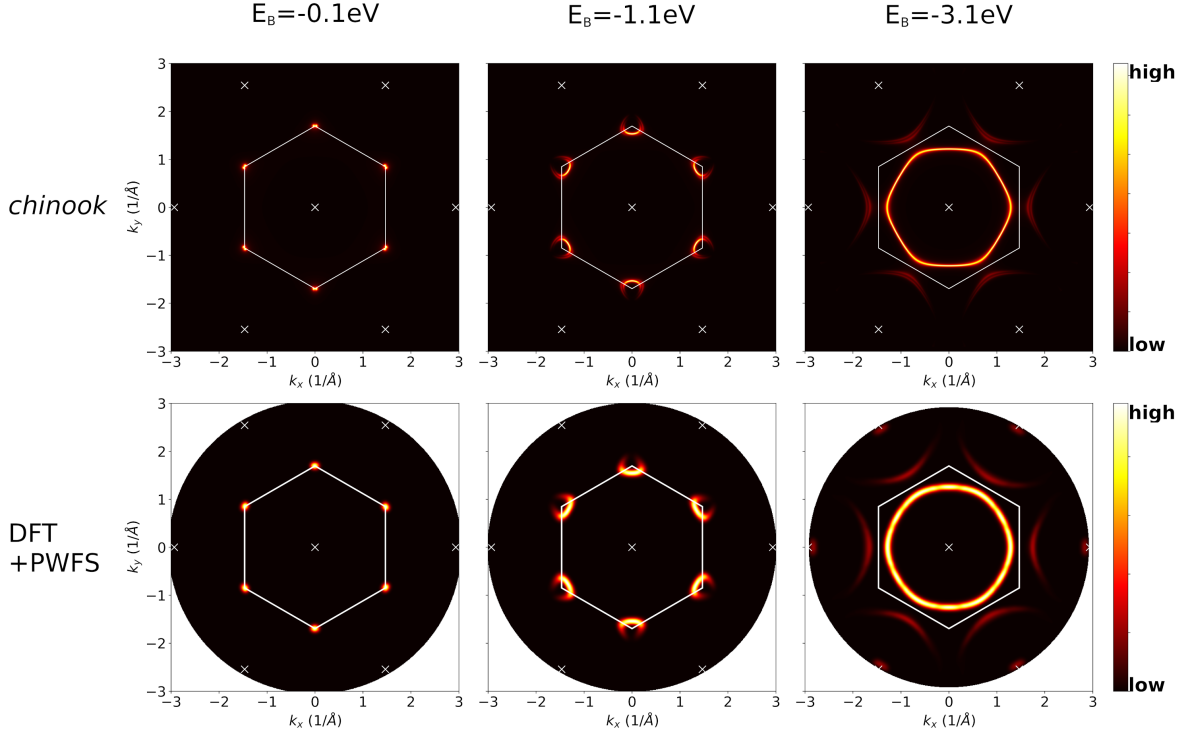


Figure 3.24: BLG-AB: ARPES momentum maps, photon energy: 40 eV; top row: maps simulated using *chinook*; bottom row: simulations DFT+PWFS approach; lines inset: boundary of the first Brillouin zone, crosses: Γ -points

details of the occupied band structure as described in the previous section. The momentum maps in Figure 3.24 again show the pockets at the K -points typical for graphene. Both types of simulations show similar structures of the pockets. Similar to BLG-AA, the pockets get contributions from two different bands. In the case here, this second band at the pockets is barely visible in the simulated maps.

The band maps in Figure 3.25 show similar results as the momentum maps in Figure 3.24. Both simulations show that only one band of the band structure (Figure 3.23b) shows a significant contributions to the photoemission. The simulations using the DFT+PWFS approach shows this band with low photoemission above the visible band.

The dependence of photoemission intensity on the photon energy in Figure 3.26 is simulated and measured the same way as described in the previous sections on SLG and BLG-AA. The results of TB calculation show the same features as in the previous sections. There is again a maximum at 28 eV photon energy with an exponential decay of the photoemission intensity to higher photon-energies. The results of the simulation using the DFT+PWFS approach for BLG-AB are comparable to the result for BLG-AA. The difference is, that here the minimum at approximately 42 eV photon energy is far less pronounced. This minimum and the subsequent maximum of the photoemission intensity simulated based on a DFT calculation is not reproduced by *chinook*.

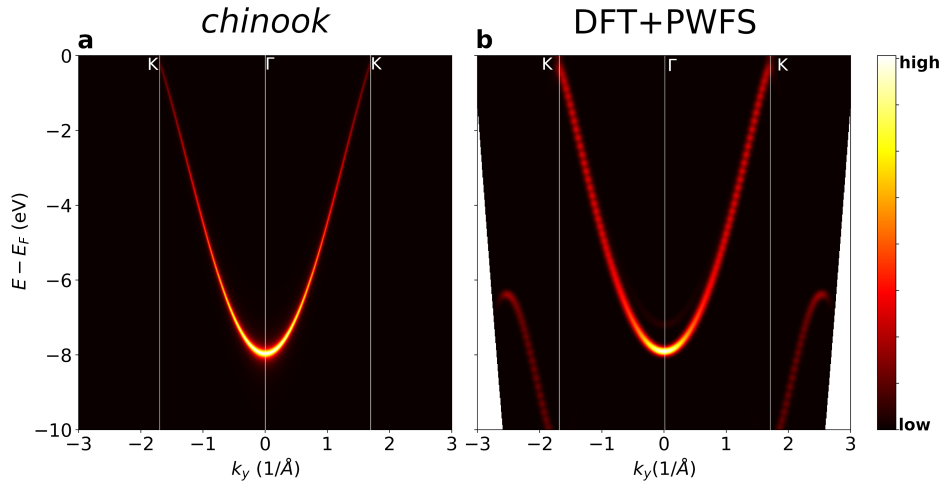


Figure 3.25: BLG-AB: ARPES band maps in ΓK -direction, photon energy: 40 eV; left panel: maps simulated using *chinook*; right panel: simulations using the DFT+PWFS approach

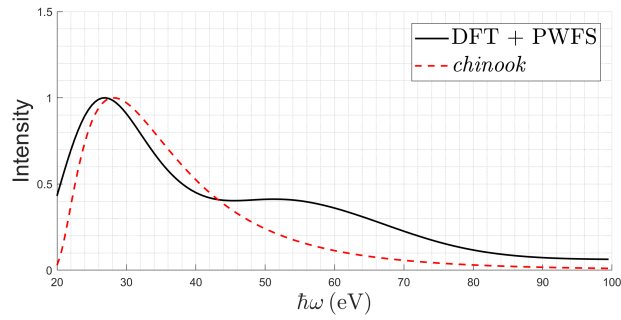


Figure 3.26: BLG-AB: photoemission intensity versus photon energy, measured for initial states $E_B = 0.1$ eV around one K -point ($1.48 \text{ \AA} \leq k_{\parallel} \leq 1.89 \text{ \AA}$)

Similar to BLG-AA, the maxima and minima in the photoemission are expected from measurements [2].

3.3.4 TB Models for BLG-AA and BLG-AB

Bilayer graphene in AA and AB stacking order are materials with a similar structure, with the difference, that for BLG-AB one graphene sublayer has a relative shift. Also the TB-models for both materials are similar, where each contains two blocks describing the single sublayer and the interactions between the sublayers (equations 3.3, 3.4). Given these similarities one may expect the interlayer hopping constants to be similar in size, which is not the case:

	d (Å)	t_2
BLG-AA	3.76	0.18
BLG-AB	3.56	0.27

The difference of the size the values for t_2 can be explained by the different layer distances, that is larger for BLG-AB. Since interlayer hopping happens only between atoms directly above each other, the shift in the layers of BLG-AB does not play a role in the size of the hopping constant.

The shift in the layers causes also a change in the electronic band structure of bilayer graphene (BLG). Figure 3.27 shows simulated band maps for BLG-AA and BLG-AB in ΓK -direction near the K -point. The band structure of BLG-AA is similar to graphene where the contributions of the sublayers are shifted relatively to each other by a small energy. In contrast, the bands of BLG-AB bend at K near the Fermi-level, so that the bands do not cross.

For free-standing BLG-AB, where the sublayers are symmetric, the band gap is zero. Under the influence of a substrate or by doping it is possible to open a band gap. The size of the gap can be controlled by changing the charge-carrier density in the sublayers of BLG-AB [2, 52].

The simulations for BLG-AA are in good agreement. Both methods predict emission from the lower lying bands and directly at the K -point is a region low photoemission intensity. Similarly, for BLG-AA only the lower lying bands contribute to the photoemission. Again, the DFT+PWFS approach predicts a region low photoemission intensity at the K -point. However, *chinook* does not show such a minimum in the emitted intensity for BLG-AA.

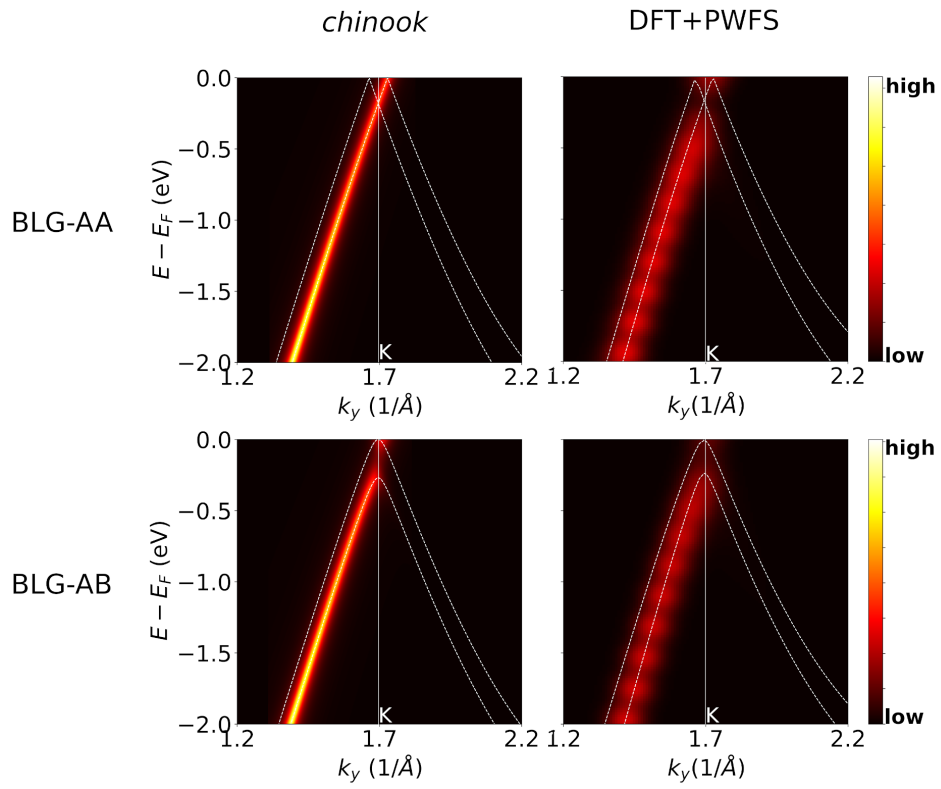


Figure 3.27: Band maps of BLG-AA and BLG-AB near K ; lines inset: band structure calculated for the respective material and method; The same parameters are used for the simulations as in the previous sections

4 Summary and Conclusion

In this thesis angle-resolved photoemission spectroscopy (ARPES) experiments are simulated for two-dimensional (2D) materials. To this end, the electronic ground state of the materials is calculated using density functional theory (DFT). Based on the Kohn-Sham orbitals obtained from DFT, ARPES is simulated within the one-step model of photoemission. The final state of the photoelectrons is treated using the plane wave final state (PWFS) approach. In this work, the PWFS approach is extended to include spin-orbit coupling (SOC).

Simulations of ARPES including SOC are done for the transition metal dichalcogenides WS_2 and WSe_2 , and for $\text{AgTe}/\text{Ag}(111)$. Important for these three materials is, that they show strong SOC. The results of the simulations are compared with experimental data from literature.

The results for the ARPES simulations for the TMDs are in good agreement with the experimental findings. Here, the calculated band structure and ARPES intensity maps coincide with the experimental data, where also the spin-splitting of the top-valence band is predicted correctly. Simulations for the spin polarization of the photoelectrons agree with expectations from the experiments. However, there are still some discrepancies regarding the distribution of the photoemission intensity, especially for WS_2 . There, the experiments show a high intensity originating from the centre of the first Brillouin zone, whereas the simulations predict a low photoemission intensity.

For $\text{AgTe}/\text{Ag}(111)$, the calculated band structure coincides with the measurements, including correct predictions for the spin-splitting at the Γ -point. However, the simulated band maps show different results for the intensity distribution compared to the experimental maps. Also, for higher photon energies, the momentum maps differ, where the angular distribution of the simulated photoemission intensity does not agree with the experiments. This leads to the conclusion, that the PWFS approach within the one-step model of photoemission is insufficient to describe the ARPES experiment for $\text{AgTe}/\text{Ag}(111)$.

Concluding from the results from the two different systems, it is possible to obtain reliable results by applying the PWFS approach to simulate ARPES for materials showing strong SOC. For these materials, including SOC in the simulations can improve the fit to experiments. But as can be seen from the calculations for $\text{AgTe}/\text{Ag}(111)$, the PWFS approach is not applicable for all systems.

In addition, calculations are also conducted for free standing films of single layer graphene (SLG) and bilayer graphene (BLG) in AA and AB stacking order. Here the ARPES simulations are performed in two modes. First, by using the PWFS approach based

on initial states modelled as Kohn-Sham orbitals (DFT+PWFS). And second, by employing a TB approach as implemented in *chinook* [12]. For the tight-binding model necessary for *chinook*, p_z orbitals are placed on each carbon atom and nearest neighbour hopping is considered. The parameters for the TB-model are obtained by fitting the TB band structure to a band structure calculated using DFT.

The band maps and momentum maps calculated using both methods show similar results. For SLG, they show Dirac cones at the K -points. For higher binding energies, the methods predict the formation of pockets around the K -points for all three systems, where the structure of the pockets is the same for both methods.

In addition to the ARPES maps, the photoemission intensity is calculated depending on the photon energy for a specific initial state near the Fermi level. For SLG both methods show a peak in intensity at a photon energy of 28 eV and a decay to higher energies, where the signal of the DFT+PWFS approach decays more slowly. The DFT+PWFS approach predicts several peaks for bilayer graphene, whereas *chinook* shows the same dependence as for SLG. The results of the DFT+PWFS approach are supported by measurements [2].

There are several advantages of *chinook* over the DFT+PWFS approach. If an accurate TB-model is available for a specific system, the simulations are numerically less expensive compared to a DFT-calculation. Therefore, larger system sizes are possible. A drawback of the TB-method is, that it needs an accurate TB-model for the system. If no such model is available, setting it up and finding the correct parameters is a difficult task, which can only be done easily for simple systems, similar to the ones used in this work. Additionally, there are some discrepancies in the results compared to the DFT+PWFS approach, where the results of the DFT+PWFS approach agree better with the experimental results.

Appendix: usage of chinook

The python package *chinook* implements a solver for a tight-binding (TB) model. Based on this TB model *chinook* can simulate angular resolved photoemission (ARPES) experiments by expanding the final state in spherical harmonics. A short description of the TB method and simulating ARPES can be found in section 2. Explanations of *chinook* are given in Ref. [12]. The python package is written by R.P. Day and is available online and via the python installer.

The following section contains a short summary on how to use *chinook* in a python script, with the example of graphene. The options and settings necessary for the program are handed to *chinook* in the form of python dictionaries.

As the first step, the libraries are imported the structure is set up. The parameters needed are the lattice vectors and the atomic positions, both are given in Cartesian coordinates in units of Å.

```
import chinook
import chinook.build_lib as build_lib
import chinook.ARPES_lib as arpes_lib
import numpy as np
import matplotlib.pyplot as plt

# lattice constant
a = 2.47
# lattice vectors
avec = np.array([[ (3**0.5)/2*a , 0.5*a , 0.0 ],
                 [ (3**0.5)/2*a , -0.5*a , 0.0 ],
                 [ 0.0 , 0.0 , 10.0 ]])

# atomic positions
p1 = np.array([0.0,0.0,0.0])
p2 = np.array([ ((1/3)**0.5)*a,0.0,0.0 ])

# possible to include SOC
spin_args = {'bool':False}#, 'soc':True, 'lam':{0:1.5}}
```

The next step combines these informations to set up the basis for the TB model. Additional information of the types of atoms and orbitals is given. The keyword 'atoms' defines labels for the atoms on each position given in 'pos', where 'Z' gives the atomic

number for the labels. 'orbs' lists the orbitals placed at each position where each orbital is characterized by the three quantum numbers of hydrogen wave-functions. '21z' stands for the $2p_z$ orbital.

```
# define the orbitals
basis_args = {'atoms':[0,0],          # number of atoms at the positions
              'Z':{0:6},             # atomic numbers
              'pos':[p1,p2],         # positions
              'orbs':[['21z'],['21z']], # orbitals at the positions
              'spin':spin_args}
```

Following, the TB Hamiltonian is defined. *chinook* accepts different ways to define the model. The main types are, first, directly giving values to the hopping integrals or, second, using Slater-Koster parameters [53]. Here the method for directly handing over the hopping integrals is presented. Since the Hamilton operator is hermitian, it is sufficient to give, for example, the upper triangular of the Hamilton matrix. The entries of the hamiltonian are given as a list, where each entry contains the two orbitals involved, the distance in Cartesian coordinates and the value of the hopping integral.

```
###Hamilton
ep = 0      # on-site energy
HP = -2.56  # hopping pz-pz

H_list=[[0,0,0,0,0,ep],
        [1,1,0,0,0,ep],
        [0,1, -1/2*((1/3)**0.5)*a , 1/2*a , 0.0 ,HP],
        [0,1, -1/2*((1/3)**0.5)*a , -1/2*a , 0.0 ,HP],
        [0,1,      ((1/3)**0.5)*a , 0.0 , 0.0 ,HP],]

hamiltonian_args = {'type':'list', # give Hamilton as list
                    'list':H_list,
                    'cutoff':0.6*a,
                    'renorm':1.0,
                    'offset':0.0,
                    'tol':1E-4,
                    'avec':avec,
                    'spin':spin_args}
```

Before doing the TB calculations, the information about required k -points are gathered in a dictionary. The points are given in units of the reciprocal lattice vectors ('pts').

```
###define Path for bandstructure plot
momentum_args = {'type':'F',
                 'avec':avec,      # real lattice
```

```

'grain':100,      # number of points
'pts':[[0,1/2,0],[0,0,0],[1/3,2/3,0]], # define path in k-space
'labels':['M','$\\Gamma$','K']} # labels for the points pts

```

Here the necessary objects will be created. `build_lib.gen_TB()` creates the TB object for *chinook*, `TB.solve_H()` then solves the TB model for the given path in momentum space and `TB.plotting()` then plots the bandstructure.

```

###create objects, solve and plot TB model
basis = build_lib.gen_basis(basis_args)
kpath = build_lib.gen_K(momentum_args)
TB = build_lib.gen_TB(basis,hamiltonian_args,kpath)
TB.solve_H()
TB.plotting()
plt.show()

```

After creating the TB object, one can use it to simulate ARPES experiments. Following are two examples, first, for a momentum map and second, for a band-map. The first lines define region in momentum space and energy, where the experiment is simulated. `arpes_args` contains the set-up for the simulation. 'cube' defines the region where the TB model is solved and ARPES is simulated, 'hv' gives the photon-energy in eV. 'pol' gives the polarization in Cartesian coordinates. 'T' gives the temperature in Kelvin, if it is positive the Fermi distribution is applied.

After defining `arpes_args` the necessary object is created with `arpes_lib.experiment()`. The calculation is started using `datacube()`. It calculates the matrix-elements in the given region in energy and momentum space. The maps are then plotted using `spectral()`. In `Imap` the command returns the photoemission intensity for each point defined in 'cube'.

Note that for plotting the momentum map the vertical axis is k and the horizontal axis represents the binding energy.

```

### ARPES
emin = -10.0
emax = 0.0 # energy range
xmin = -3.0
xmax = 3.0 # region in kx-direction
ymin = -3.0
ymax = 3.0 # region in ky-direction
nk = 300 # number of points in k-space
nE = 300 # number of energy-points

# momentum map
arpes_args={'cube':{'X':[xmin,xmax,nk]},

```

```

        'Y':[ymin,ymax,nk],
        'kz':0.0,
        'E':[-3.1,-0.1,7]},# region in x,y,E to solve TB
    'SE':['constant',0.1], # self energy
    'hv': 30, # photon energy
    'pol':np.array([0,0,1]),# light polarization in z direction
    'resolution':{'E':0.08,'k':0.045},
    'T':-1.0, # Temperature, -1: off
    'W':4.282, # work function
    'rad_type':'slater'} # type of radial integrals

experiment = arpes_lib.experiment(TB,arpes_args)
experiment.datacube()
Imap,Imap_resolution,axes = experiment.spectral(ARPES_dict=arpes_args,
        slice_select=('E', -0.1),
        plot_bands=False); # select k-map for EB=-0.1
plt.show()

# band map ky
arpes_args={'cube':{'X':[-0.001,0.001,3],
        'Y':[ymin,ymax,nk],
        'kz':0.0,
        'E':[emin,emax,nE]},# region in x,y,E to solve TB
    'SE':['constant',0.1], # self energy
    'hv': 30.0, # photon energy
    'pol':np.array([0,0,1]),# light polarization in z direction
    'resolution':{'E':0.08,'k':0.045},
    'T':-1.0, # Temperature, -1: off
    'W':4.282, # work function
    'rad_type':'slater'} # type of radial integrals

experiment = arpes_lib.experiment(TB,arpes_args)
experiment.datacube()
Imap,Imap_resolution,axes = experiment.spectral(ARPES_dict=arpes_args,
        slice_select=('x', 0.0),
        plot_bands=False); # select band-map for kx=const.
plt.show()

```

Bibliography

- [1] F. D. M. Haldane. Model for a quantum hall effect without landau levels: Condensed-matter realization of the "parity anomaly". *Physical Review Letters*, 61:2015–2018, Oct 1988.
- [2] Taisuke Ohta, Aaron Bostwick, Jessica L McChesney, Thomas Seyller, Karsten Horn, and Eli Rotenberg. Interlayer interaction and electronic screening in multi-layer graphene investigated with angle-resolved photoemission spectroscopy. *Physical Review Letters*, 98(20):206802, 2007.
- [3] C. Ataca, H. Sahin, and S. Ciraci. Stable, single-layer MX_2 transition-metal oxides and dichalcogenides in a honeycomb-like structure. *The Journal of Physical Chemistry C*, 116(16):8983–8999, 2012.
- [4] Thang Phan Nguyen, Woonbae Sohn, Jeong Hyeon Oh, Ho Won Jang, and Soo Young Kim. Size-dependent properties of two-dimensional MoS_2 and WS_2 . *The Journal of Physical Chemistry C*, 120(18):10078–10085, 2016.
- [5] Jiadong Zhou, Junhao Lin, Xiangwei Huang, Yao Zhou, Yu Chen, Juan Xia, Hong Wang, Yu Xie, Huimei Yu, Jincheng Lei, et al. A library of atomically thin metal chalcogenides. *Nature*, 556(7701):355–359, 2018.
- [6] Zhiyong Y. Zhu, Yingchun C. Cheng, and Udo Schwingenschlögl. Giant spin-orbit-induced spin splitting in two-dimensional transition-metal dichalcogenide semiconductors. *Physical Review B*, 84(15):153402, 2011.
- [7] Iori Tanabe, Takashi Komesu, Duy Le, Takat B. Rawal, Eike F. Schwier, Mingtian Zheng, Yohei Kojima, Hideaki Iwasawa, Kenya Shimada, Talat S. Rahman, et al. The symmetry-resolved electronic structure of $2H\text{-WSe}_2$ (0001). *Journal of Physics: Condensed Matter*, 28(34):345503, 2016.
- [8] P. Chen, Woei Wu Pai, Y.H. Chan, W.L. Sun, C.Z. Xu, D.S. Lin, M.Y. Chou, A.V. Fedorov, and T.C. Chiang. Large quantum-spin-hall gap in single-layer $1T'$ WSe_2 . *Nature communications*, 9(1):1–7, 2018.
- [9] Peter Puschnig and Daniel Lüftner. Simulation of angle-resolved photoemission spectra by approximating the final state by a plane wave: From graphene to polycyclic aromatic hydrocarbon molecules. *Journal of Electron Spectroscopy and Related Phenomena*, 200:193–208, 2015. Special Anniversary Issue: Volume 200.

- [10] Daniel Lüftner, Simon Weiß, Xiaosheng Yang, Philipp Hurdax, Vitaliy Feyer, Alexander Gottwald, Georg Koller, Serguei Soubatch, Peter Puschnig, Michael G. Ramsey, and F. Stefan Tautz. Understanding the photoemission distribution of strongly interacting two-dimensional overlayers. *Physical Review B*, 96:125402, Sep 2017.
- [11] Xiaosheng Yang, Larissa Egger, Jana Fuchsberger, Martin Unzog, Daniel Lüftner, Felix Hajek, Philipp Hurdax, Matteo Jugovac, Giovanni Zamborlini, Vitaliy Feyer, Georg Koller, Peter Puschnig, F. Stefan Tautz, Michael G. Ramsey, and Serguei Soubatch. Coexisting charge states in a unary organic monolayer film on a metal. *The Journal of Physical Chemistry Letters*, 10(21):6438–6445, 2019. PMID: 31573816.
- [12] Ryan P. Day, Berend Zwartsenberg, Ilya S. Elfimov, and Andrea Damascelli. Computational framework *chinook* for angle-resolved photoemission spectroscopy. *npj Quantum Materials*, 4(1):1–10, 2019.
- [13] Peter Puschnig, Stephen Berkebile, Alexander J. Fleming, Georg Koller, Konstantin Emtsev, Thomas Seyller, John D. Riley, Claudia Ambrosch-Draxl, Falko P. Netzer, and Michael G. Ramsey. Reconstruction of molecular orbital densities from photoemission data. *Science*, 326(5953):702–706, 2009.
- [14] P. Puschnig and M.G. Ramsey. Photoemission tomography: Valence band photoemission as a quantitative method for investigating molecular films. In Klaus Wandelt, editor, *Encyclopedia of Interfacial Chemistry*, pages 380 – 391. Elsevier, Oxford, 2018.
- [15] Dominik Brandstetter, Xiaosheng Yang, Daniel Lüftner, F. Stefan Tautz, and Peter Puschnig. kmap.py: A python program for simulation and data analysis in photoemission tomography. *Computer Physics Communications*, 263:107905, 2021.
- [16] G. Kresse and J. Hafner. Ab initio molecular dynamics for liquid metals. *Physical Review B*, 47:558–561, Jan 1993.
- [17] G. Kresse and J. Furthmüller. Efficient iterative schemes for *ab initio* total-energy calculations using a plane-wave basis set. *Physical Review B*, 54:11169–11186, Oct 1996.
- [18] M. Born and R. Oppenheimer. Zur Quantentheorie der Molekeln. *Annalen der Physik*, 389(20):457–484, 1927.
- [19] P. Hohenberg and W. Kohn. Inhomogeneous electron gas. *Physical Review*, 136:B864–B871, Nov 1964.
- [20] W. Kohn and L. J. Sham. Self-consistent equations including exchange and correlation effects. *Physical Review*, 140:A1133–A1138, Nov 1965.

- [21] Peter Puschnig. Lecture notes: "Fundamentals of Electronic Structure Theory". <https://physik.uni-graz.at/~pep/FEST/FEST.pdf>. Last accessed 2021-01-04.
- [22] J. P. Perdew, K. Burke, and M. Ernzerhof. Generalized Gradient Approximation Made Simple. *Physical Review Letters*, 77:3865–3868, 1996.
- [23] Felix Bloch. Über die Quantenmechanik der Elektronen in Kristallgittern. *Zeitschrift für Physik*, 52(7):555–600, July 1929.
- [24] Neil W. Ashcroft and N. David Mermin. *Solid State Physics*. New York: Holt, Rinehart and Winston,, 1976.
- [25] Peter E. Blöchl. Projector augmented-wave method. *Physical Review B*, 50(24):17953, 1994.
- [26] C. Itzykson and J.-B. Zuber. *Quantum Field Theory*. McGraw-Hill, New York, 1980.
- [27] E. van Lenthe, Evert-Jan Baerends, and Jaap G. Snijders. Relativistic regular two-component hamiltonians. *The Journal of chemical physics*, 99(6):4597–4610, 1993.
- [28] Soner Steiner, Sergii Khmelevskyi, Martijn Marsmann, and Georg Kresse. Calculation of the magnetic anisotropy with projected-augmented-wave methodology and the case study of disordered $\text{Fe}_{1-x}\text{Co}_x$ alloys. *Physical Review B*, 93(22):224425, 2016.
- [29] D Hobbs, G Kresse, and J Hafner. Fully unconstrained noncollinear magnetism within the projector augmented-wave method. *Physical Review B*, 62(17):11556, 2000.
- [30] J. Kübler, K.-H. Höck, and A. R. Williams. Density functional theory of non-collinear magnetism. *Journal of Physics F: Metal Physics*, 18:469–483, 1988.
- [31] G Dresselhaus, Mildred S. Dresselhaus, and Riichiro Saito. *Physical properties of carbon nanotubes*. World scientific, 1998.
- [32] Peter J. Feibelman and D. E. Eastman. Photoemission spectroscopy—correspondence between quantum theory and experimental phenomenology. *Physical Review B*, 10:4932–4947, Dec 1974.
- [33] Daniel Lüftner. *Orbital tomography: Understanding photoemission of organic molecular films*. PhD thesis, Citeseer, 2015.
- [34] Albert Einstein. Über einen die Erzeugung und Verwandlung des Lichtes betreffenden heuristischen Gesichtspunkt. *Annalen der Physik*, 322(6):132–148, 1905.
- [35] Gerd Schönhense. Circular dichroism and spin polarization in photoemission from adsorbates and non-magnetic solids. *Physica Scripta*, T31:255–275, jan 1990.

- [36] R. Mehrem. The plane wave expansion, infinite integrals and identities involving spherical bessel functions. *Applied Mathematics and Computation*, 217(12):5360 – 5365, 2011.
- [37] Maciej Dendzik, Matteo Michiardi, Charlotte Sanders, Marco Bianchi, Jill A. Miwa, Signe S Grønberg, Jeppe V. Lauritsen, Albert Bruix, Bjørk Hammer, and Philip Hofmann. Growth and electronic structure of epitaxial single-layer WS₂ on Au (111). *Physical Review B*, 92(24):245442, 2015.
- [38] W.J. Schutte, J.L. De Boer, and F. Jellinek. Crystal structures of tungsten disulfide and diselenide. *Journal of Solid State Chemistry*, 70(2):207 – 209, 1987.
- [39] Sung-Kwan Mo, Choongyu Hwang, Yi Zhang, Mauro Fanciulli, Stefan Muff, J Hugo Dil, Zhi-Xun Shen, and Zahid Hussain. Spin-resolved photoemission study of epitaxially grown MoSe₂ and WSe₂ thin films. *Journal of physics: Condensed matter*, 28(45):454001, 2016.
- [40] Yi Zhang, Miguel M. Ugeda, Chenhao Jin, Su-Fei Shi, Aaron J. Bradley, Ana Martín-Recio, Hyejin Ryu, Jonghwan Kim, Shujie Tang, Yeongkwan Kim, et al. Electronic structure, surface doping, and optical response in epitaxial WSe₂ thin films. *Nano letters*, 16(4):2485–2491, 2016.
- [41] Hugo Henck, Zeineb Ben Aziza, Debora Pierucci, Feriel Laourine, Francesco Reale, Pawel Palczynski, Julien Chaste, Mathieu G Silly, François Bertran, Patrick Le Fevre, et al. Electronic band structure of two-dimensional WS₂/graphene van der waals heterostructures. *Physical Review B*, 97(15):155421, 2018.
- [42] Søren Ulstrup, Jyoti Katoch, Roland J. Koch, Daniel Schwarz, Simranjeet Singh, Kathleen M. McCreary, Hyang Keun Yoo, Jinsong Xu, Berend T. Jonker, Roland K. Kawakami, et al. Spatially resolved electronic properties of single-layer WS₂ on transition metal oxides. *ACS nano*, 10(11):10058–10067, 2016.
- [43] Duy Le, Alexei Barinov, Edwin Preciado, Miguel Isarraraz, Iori Tanabe, Takashi Komesu, Conrad Troha, Ludwig Bartels, Talat S. Rahman, and Peter A. Dowben. Spin-orbit coupling in the band structure of monolayer WSe₂. *Journal of Physics: Condensed Matter*, 27(18):182201, 2015.
- [44] Umberto De Giovannini, Hannes Hübener, and Angel Rubio. A first-principles time-dependent density functional theory framework for spin and time-resolved angular-resolved photoelectron spectroscopy in periodic systems. *Journal of Chemical Theory and Computation*, 13(1):265–273, Dec 2016.
- [45] Maximilian Ünzelmann, Hendrik Bentmann, Philipp Eck, Tilman Kießlinger, Begmuhammet Geldiyev, Janek Rieger, Simon Moser, Raphael C. Vidal, Katharina Kießner, Lutz Hammer, M. Alexander Schneider, Thomas Fauster, Giorgio Sangiovanni, Domenico Di Sante, and Friedrich Reinert. Orbital-driven rashba effect in a binary honeycomb monolayer agte. *Physical Review Letters*, 124:176401, Apr 2020.

- [46] Yu A Bychkov and É I Rashba. Properties of a 2D electron gas with lifted spectral degeneracy. *JETP Lett*, 39(2):78, 1984.
- [47] Philipp Haas, Fabien Tran, and Peter Blaha. Erratum: Calculation of the lattice constant of solids with semilocal functionals. *Physical Review B*, 79:209902, May 2009.
- [48] A description of the method of simulated annealing can be found in the lecture notes: "Computer Simulation" by Prof. H.G. Evertz. <https://itp.tugraz.at/~evertz/Computersimulations/cs2020.pdf>. Last accessed 2020-12-13.
- [49] Simon Moser. An experimentalist's guide to the matrix element in angle resolved photoemission. *Journal of Electron Spectroscopy and Related Phenomena*, 214:29 – 52, 2017.
- [50] S. Weiß, D. Lüftner, T. Ules, E.M. Reinisch, H. Kaser, A. Gottwald, M. Richter, S. Soubatch, G. Koller, M.G. Ramsey, et al. Exploring three-dimensional orbital imaging with energy-dependent photoemission tomography. *Nature communications*, 6(1):1–8, 2015.
- [51] Stefan Grimme, Jens Antony, Stephan Ehrlich, and Helge Krieg. A consistent and accurate *ab initio* parametrization of density functional dispersion correction (DFT-D) for the 94 elements H-Pu. *The Journal of Chemical Physics*, 132(15):154104, 2010.
- [52] Taisuke Ohta, Aaron Bostwick, Thomas Seyller, Karsten Horn, and Eli Rotenberg. Controlling the electronic structure of bilayer graphene. *Science*, 313(5789):951–954, 2006.
- [53] John C Slater and George F Koster. Simplified LCAO method for the periodic potential problem. *Physical Review*, 94(6):1498, 1954.